

SLOVAK UNIVERSITY OF TECHNOLOGY IN BRATISLAVA

Faculty of Civil Engineering

Reg. No.: SvF-13415-28298

## **Numerical method in geodesy**

Dissertation thesis

2014

Ing. Marek Macák

SLOVAK UNIVERSITY OF TECHNOLOGY IN BRATISLAVA

Faculty of Civil Engineering

Reg. No.: SvF-13415-28298

## **Numerical method in geodesy**

Dissertation thesis

Study programme: Applied Mathematics

Study field number: 1114

Study field: 9.1.9 Applied Mathematics

Training workplace: Department of Mathematics and Constructive Geometry

Thesis supervisor: prof. RNDr. Karol Mikula, DrSc.

**Bratislava 2014**

**Ing. Marek Macák**

## Acknowledgement

I owe prof. RNDr. Karol Mikula, DrSc. a debt of gratitude for his patient guidance in the numerical world and many worthwhile talks and advices during the whole study.

I am grateful to my consultant Ing. Zuzana Minarechová, PhD. for his support and my special thank belongs also to Ing. Róbert Čunderlík, PhD. for his comments, suggestions and help.

I am thankful to wife Mária, my family, friends and colleagues.

**Declaration of Authorship:**

I hereby certify to have written this thesis myself, using the literature cited.

Bratislava, 30. 5. 2014

.....

Ing. Marek Macák



## ZADANIE DIZERTAČNEJ PRÁCE

Evidenčné číslo:	SvF-13415-28298
ID študenta:	28298
Autor práce:	Ing. Marek Macák (28298)
Študijný program:	aplikovaná matematika
Študijný odbor:	9.1.9 aplikovaná matematika
Vedúci práce:	prof. RNDr. Karol Mikula, DrSc.
Externá vzdelávacia inštitúcia:	0

Názov témy: **Numerické metódy v geovedách**

Špecifikácia zadania:

Dizertačná práca sa zaoberá návrhom nových numerických metód na riešenie geodetických okrajových úloh. Na diskretizáciu Laplaceovej rovnice v 3D bude použitá metóda konečných objemov a bude vytvorená jej efektívna paralelná implementácia. Numerické metódy budú vybudované pre geodetické okrajové úlohy s Neumannovou okrajovou podmienkou, s okrajovou podmienkou v tvare šikmej derivácie a pre nelineárnu okrajovú podmienku pre normu gradientu riešenia. Vytvorené numerické schémy budú testované na reprezentatívnych príkladoch, bude získaný ich experimentálny rád konvergenzie a budú aplikované vo výpočtoch tiažového poľa Zeme pomocou riešenia geodetických okrajových úloh.

Dátum zadania dizertačnej práce: 02.09.2010

Termín odovzdania dizertačnej práce: 31.05.2014

**Ing. Marek Macák**

riešiteľ

**prof. RNDr. Radko Mesiar, DrSc.**

vedúci pracoviska

**prof. RNDr. Radko Mesiar, DrSc.**

garant študijného programu

## POKYNY na vypracovanie dizerta nej práce

### Úvodné ustanovenie

V zmysle zákona . 131/2002 Z. z. o vysokých školách a o zmene a doplnení niektorých zákonov v znení neskorších predpisov je sú as ou štúdia pod a každého študijného programu aj závere ná práca. Jej obhajoba patrí medzi štátne skúšky. Závere nou prácou pri štúdiu pod a študijného programu tretieho stup a je dizerta ná práca. Podkladom na vypracovanie dizerta nej práce je zadanie dizerta nej práce

### Štruktúra závere nej práce

- titulný list,
- zadanie závere nej práce,
- pokyny na vypracovanie,
- vyhlásenie autora,
- názov a abstrakt v slovenskom aj anglickom jazyku (spolu v rozsahu jednej strany),
- obsah s o íslovaním kapitol,
- zoznam príloh,
- zoznam ilustrácií a zoznam tabuliek,
- zoznam skratiek a zna iek,
- text samotnej práce,
  - úvod,
  - sú asný stav riešenej problematiky,
  - ciele závere nej práce,
  - metodika práce a metódy skúmania,
  - výsledky práce a diskusia,
  - záver (stru né zhrnutie dosiahnutých výsledkov vo vz ahu k stanoveným cie om),
- resumé (len ak je práca vypracovaná v inom ako štátnom jazyku),
- zoznam použitej literatúry,
- prílohy (výkresy, tabu ky, mapy, ná rty) vrátane postera s rozmermi 1000x700 mm.
- autoreferát (spracovaný v zmysle Študijného poriadku STU v Bratislave).

### Rozsah a forma

1. Obsah a forma závere nej práce musí by spracovaná v zmysle vyhlášky MŠVVaŠ SR . 233/2011 Z. z., ktorou sa vykonávajú niektoré ustanovenia zákona . 131/2002 Z. z. a v zmysle Metodického usmernenia . 56/2011 o náležitostiach závere ných prác.
2. Odporú aný rozsah závere nej práce je 80 až 120 strán. Práca sa odovzdáva v štyroch vyhotoveniach. Práca musí by viazaná v pevnej väzbe (nie hrebe ovej) tak, aby sa jednotlivé listy nedali vybera .
3. Autor práce je povinný vloži prácu v elektronickej forme do akademického informa ného systému. Autor zodpovedá za zhodu listinného aj elektronickeho vyhotovenia.

4. Po vložení závere nej práce do informa ného systému, predloží autor fakulte ním podpísaný návrh licen nej zmluvy. Návrh licen nej zmluvy je vytvorený akademickým informa ným systémom.
5. Odporú aný typ písma je Times New Roman, ve kos 12 a je jednotný v celej práci. Odporú ané nastavenie strany - riadkovanie 1,5, okraj vnútorný 3,5 cm, vonkajší 2 cm, zhora a zdola 2,5 cm, orientácia na výšku, formát A4.
6. Obrázky a vzorce sa íslujú v rámci jednotlivých kapitol (napr. obr. 3.1 je obrázok . 1 v kapitole 3). Vzorce sa íslujú na pravom okraji riadku v okrúhlych zátvorkách - napr. (3.1).
7. Všetky výpo ty musia by usporiadané tak, aby bolo možné preveri ich správnos .
8. Pri všetkých prevzatých vzorcoch, tabu kách, citovaných astiach textu musí by uvedený prame .
9. Citovanie literatúry vrátane elektronických materiálov sa uvádza pod a STN ISO 690 (01 0197) : 2012. *Informácie a dokumentácia. Návod na tvorbu bibliografických odkazov na informa né pramene a ich citovanie.*
10. Príklad zoznamu bibliografických odkazov:
  - ABELOVI , J. a kol.: *Meranie v geodetických sie ach.* Bratislava, Alfa 1990, ISBN 0-1554-9173.
  - MICHAL ÁK, O. – ADLER, E.: Výskum stability dunajských hrádzí. In: *Zborník vedeckých prác Stavebnej fakulty SVŠT.* Bratislava: Edi né stredisko SVŠT 1976, s. 18-28. ISBN 0-3552-5214.
  - ŠÜTTI, J.: Ur ovanie priestorových posunov stavebných objektov. *Geodetický kartografický obzor.* 2000, ro . 2, . 3, s. 8-16. ISSN 0811-6900.
  - Article 18. Technical Cooperation. <http://www.lac.uk/iso/tc456> (2013-09-28)
11. Za jazykovú a terminologickú správnos závere nej práce zodpovedá študent.
12. Autoreferát má formát A5, rozsah najviac 20 strán.
13. Formu postera (elektronická alebo aj tla ená) ur í garant študijného programu.
14. Vzor pre poster je uvedený na dokumentovom serveri v akademickom informa nom systéme univerzity.

.....  
 podpis garanta študijného programu

Ustanovenia týchto pokynov som vzal na vedomie. Som si vedomý(á), že ak nebude moja závere ná práca vypracovaná v súlade s týmito pokynmi, nebude prijatá na obhajobu.

V Bratislave .....

.....  
 podpis študenta

## Abstrakt

Dizertačná práca sa zaoberá riešením geodetickej okrajovej úlohy (GOU) pomocou nových prístupov a numerických schém. Je v nej vybudovaná efektívna paralelná metóda na riešenie GOU s Neumannovou okrajovou podmienkou pomocou metódy konečných objemov. Ďalej prezentuje dva nové prístupy k riešeniu GOU so šikmou deriváciou. Prvý prístup je založený na rozklade gradientu na normálovú a tangenciálnu zložku, druhý je založený na chápaní okrajovej podmienky ako rovnice advekcie. Nakoniec sa zaoberáme návrhom iteračného spôsobu riešenia nelineárnej GOU.

**Kľúčové slová:** geodetická okrajová úloha, metóda konečných objemov, okrajová úloha so šikmou deriváciou, centrálna schéma, up-wind schéma, paralelné výpočty

## Abstract

The PhD. thesis deals with a solution to the geodetic boundary value problems (GBVP) involving new approaches and schemes. Namely, we have developed an efficient parallel approach to solving the GBVP with the Neumann boundary condition (BC) by the finite volume method. Then we have presented two new approaches for solving the GBVP with the oblique derivative BC. The first approach is based on a decomposition of the gradient into the normal and tangential directions, while the second one treats the oblique derivative BC as an advection equation. Finally, we deal with an iterative approach for solving the non-linear GBVP.

**Keywords:** geodetic boundary value problems, finite volume method, oblique derivative boundary condition, central scheme, up-wind scheme, parallel computations

# Contents

<b>List of Figures</b>	<b>12</b>
<b>List of Tables</b>	<b>14</b>
<b>List of shortcuts</b>	<b>15</b>
<b>Introduction</b>	<b>17</b>
<b>1 Formulation of the geodetic boundary value problems</b>	<b>20</b>
1.1 Historical background . . . . .	20
1.2 The Earth's gravity field . . . . .	24
1.3 The geodetic boundary value problems . . . . .	29
1.4 Numerical approaches for solving GBVP . . . . .	35
<b>2 Numerical solution of the Neumann boundary-value problem</b>	<b>37</b>
2.1 The finite volume method . . . . .	37
2.1.1 Transmissivity coefficients for spherical domains . . . . .	39
2.1.2 Transmissivity coefficients for ellipsoidal domains . . . . .	40
2.1.3 Iterative solvers . . . . .	41
2.1.4 Parallelization of the method . . . . .	43
2.2 Numerical experiments . . . . .	45
2.2.1 Theoretical numerical experiments and experimental order of convergence . . . . .	46
2.2.2 Comparison of FVM solutions using spherical and ellipsoidal Earth's approximation . . . . .	47
2.2.3 Global and local gravity field modelling . . . . .	48
<b>3 Numerical solution of the oblique derivative boundary-value problem</b>	<b>54</b>
3.1 The central scheme for solving the oblique derivative BVP . . . . .	54
3.1.1 2D case . . . . .	55
3.1.2 3D case . . . . .	57

3.2	Numerical experiments using the central scheme . . . . .	60
3.2.1	2D Case . . . . .	60
3.2.2	3D Case . . . . .	61
3.2.3	3D numerical experiments with real data . . . . .	64
3.2.4	A possible problems arising in the central scheme . . . . .	65
3.3	The up-wind scheme for solving oblique derivative BVP . . . . .	67
3.4	Numerical experiments using the up-wind scheme . . . . .	69
3.4.1	2D Case . . . . .	70
3.4.2	3D Case . . . . .	71
3.4.3	3D numerical experiments with real data . . . . .	72
<b>4</b>	<b>On an iterative approach to solving the non-linear geodetic boundary-value problem</b>	<b>75</b>
4.1	Numerical experiments . . . . .	76
4.1.1	2D Case . . . . .	76
4.1.2	3D Case . . . . .	76
4.1.3	3D numerical experiments with real data . . . . .	78
	<b>Conclusions</b>	<b>82</b>
	<b>Resumé</b>	<b>84</b>
	<b>Bibliography</b>	<b>88</b>
	<b>The author's publications</b>	<b>94</b>

# List of Figures

1.1.1	Illustration of the different approaches a) Stokes approach b) Molodensky approach, where $H^*$ is the normal height, $H$ is the orthometric height, $h$ is the geometric height, $\zeta$ is the height anomaly and $N$ is the geoid undulation [54]. . . . .	23
1.2.1	Rectangular and spherical coordinates [54]. . . . .	24
1.2.2	Level surfaces and the geoid [54]. . . . .	27
1.2.3	Geoid and reference ellipsoid [54]. . . . .	28
1.3.1	Plots of the bounded domain $\Omega$ : a) local, b) global case. The part of the boundary $\Gamma$ represents the Earth surface and is plotted in green. Artificial boundaries are plotted in black (upper spherical part) and in blue (planar sides of the domain in case $a$ ). . . . .	34
2.1.1	Illustration of the grid ( $n_1 = 3, n_2 = 4, n_3 = 5$ ). a) Horizontal cut b) Vertical cut in zonal direction c) Vertical cut in meridional direction d) 3D view. The volume $p$ is hatched by dots, while its adjacent volumes $q$ are hatched by dashed lines. . . . .	38
2.1.2	Different types for data splitting and overlapping over parallel processes. a) Radial split of domain b) Meridional split of domain. . . . .	45
2.2.1	Himalayas: a) The disturbing potential solution $T[m^2.s^{-2}]$ above Himalayas computed by the FVM. b) residuals $T[m^2.s^{-2}]$ between the ellipsoidal FVM solution and the disturbing potential generated directly from EGM2008 on the bottom boundary $\Gamma$ . c) residuals $T[m^2.s^{-2}]$ between the spherical FVM solution and EGM2008 solution. . . . .	49
2.2.2	Earth: The disturbing potential solution $T[m^2.s^{-2}]$ computed by FVM. . . . .	50
2.2.3	Earth: Residuals $T[m^2.s^{-2}]$ between the disturbing potential computed by the FVM and EGM2008 solution on the bottom boundary $\Gamma$ . . . . .	51
2.2.4	SR: Quasigeoid model $\zeta[m]$ in the area of the Slovak Republic obtained by solving the Neumann FGBVP. Red crosses denote the distribution of 61 GPS/leveling points. . . . .	53

3.1.1	Illustration of the 2D computational grid for an approximation of the oblique derivative. a) $\mathbf{x}_P$ denotes position vector of the center of volume $p$ . b) $T_P$ denotes the value of the disturbing potential in the center of finite volume $p$ . Vector $\vec{t}$ denote tangent vector and $\vec{n}$ the normal vector to $\Gamma$ . . . . .	56
3.1.2	Illustration of the 3D computational grid for an approximation of the oblique derivative. a) $\mathbf{x}_P$ denotes position vector of the center of volume $p$ . b) $T_P$ denotes the value of the disturbing potential in the center of finite volume $p$ . Vectors $\vec{t}_1$ and $\vec{t}_2$ denote linearly independent tangent vectors to $\Gamma$ and $\vec{n}$ the normal vector to $\Gamma$ . . . . .	59
3.2.1	Graphs of the 2D solution to BVP with a) the Neumann BC b) the oblique derivative BC. . . . .	61
3.2.2	Illustration of creating $\vec{s}$ by rotating of $\vec{s}_1$ in 2D on the bottom boundary $\Gamma$ . . . . .	62
3.2.3	Earth: Differences $T[m^2.s^{-2}]$ between solutions to the GBVP with the oblique derivative BC and the Neumann BC. . . . .	65
3.2.4	SR: The differences in quasigeoidal heights $\zeta[m]$ obtained as a solution to the FGBVP with the oblique derivative BC and solution to the FGBVP with the Neumann BC. . . . .	66
3.2.5	Illustration of creating $\vec{s}$ by rotating of $\vec{s}_1$ by an angle $\pm\alpha$ in 2D case. . . . .	67
3.3.1	Illustration of the 2D FVM grid. The dashed lines denote the boundaries of added finite volumes, by blue colour is depicted the volume of interest and by green its neighbours. The vectors $\vec{s}$ are depicted by red. . . . .	70
3.4.1	Earth: Residuals of the disturbing potential $T[m^2.s^{-2}]$ between the FVM solution obtained by implementing the central scheme and the FVM solution obtained by implementing up-wind scheme. . . . .	73
3.4.2	SR: Differences in the quasigeoidal heights $\zeta[m]$ between the up-wind scheme and the central scheme. . . . .	74
4.1.1	a) Illustration of possible oscillation in central scheme iterative solution. b) Illustration of the solution obtained by up-wind scheme, <i>Exp.</i> 3.2.2. . . . .	77
4.1.2	Earth: Differences in $T[m^2.s^{-2}]$ between $10^{th}$ and $1^{st}$ iteration, representing the numerically obtained linearization error. . . . .	79
4.1.3	SR: Differences in $\zeta[m]$ between the $10^{th}$ and $1^{st}$ iteration obtained by solving the NSFGBVP. . . . .	80

# List of Tables

2.1	Efficiency comparison of the stationary and nonstationary methods in the experiment with size $n_1 \times n_2 \times n_3 = 500 \times 300 \times 100$ , tested on one processor. . . . .	42
2.2	The average memory and time costs for various BiCG linear solvers, where APXY is a number of vector scalar products, DOT is a number of scalar-vector multiplications, MEM represents a number of additional vectors needed in iterative procedure, ITER gives a number of iterations to reach the prescribed residual and TIME presents the overall CPU time in seconds. The table is constructed for a particular nonsymmetric matrix from our finite volume method, and from MEM and TIME columns one can see optimality of Bi-CGSTAB. BiCGstab( $l$ ) denotes Bi-CGSTAB restarted at each $l^{th}$ step [47]. . . . .	42
2.3	Comparison of communication memory cost (in MB) for different data splitting in two numerical experiments. . . . .	44
2.4	The $L_2(\Omega)$ -norm and the EOC of differences between the exact solution $T^*$ and FVM solutions $T$ for the <i>Exp.</i> 2.2.1 with Neumann BC in a domain between two spheres. . . . .	46
2.5	The $L_2(\Omega)$ -norm and the EOC of differences between the exact solution $T^*$ and FVM solutions $T$ for the <i>Exp.</i> 2.2.2 with Neumann BC in a tesseroidal domain. . . . .	47
2.6	Himalayas: Comparison of statistical characteristics for spherical and ellipsoidal domains [ $m^2s^{-2}$ ]. . . . .	48
2.7	Earth: Statistics of residuals $T[m^2s^{-2}]$ on the bottom boundary $\Gamma$ . TOTAL means statistics for the whole computational domain, SEA means statistics only over the sea and LAND means statistics over the lands. . . . .	51
2.8	SR: The GPS/leveling test [ $m$ ] at 61 points in area of Slovakia, where <i>FEM</i> denotes the solution presented in [13], <i>BEM</i> the solution published in [10] and <i>FFT (gravsoft)</i> denotes the solution presented in [39]. All solutions are obtained without applying the fitting method. . . . .	52
3.1	Conversion between the mesh index and the compass notation. . . . .	55
3.2	The $L_2(\Omega)$ -norm and the EOC for the <i>Exp.</i> 3.2.1 with the oblique derivative BC computed with the shifted point mass source $\mathbf{x}_C = (0.5, 0.35)$ . . . . .	61

3.3	The $L_2(\Omega)$ -norm and the EOC for the <i>Exp.</i> 3.2.2 with the oblique derivative BC when the oblique vector $\vec{s}$ does not have direction of the solution gradient. . . . .	62
3.4	The $L_2(\Omega)$ -norm and the EOC for the <i>Exp.</i> 3.2.3 with oblique derivative BC computed from shifted point mass source $\mathbf{x}_C = (-0.2, 0.1, 0.05)$ . . .	63
3.5	The $L_2(\Omega)$ -norm and the EOC for the <i>Exp.</i> 3.2.4 with the oblique derivative BC when the oblique vector $\vec{s}$ does not have direction of the solution gradient. . . . .	63
3.6	Earth: Statistics of residuals $T[m^2s^{-2}]$ on the bottom boundary $\Gamma$ between solutions to the GBVP with the oblique derivative BC and the Neumann BC. . . . .	64
3.7	SR: The GPS/leveling test $[m]$ at 61 points in area of Slovakia. . . . .	65
3.8	The $L_2(\Omega)$ -norm, the $MAX(\Gamma)$ -norm and the EOC for the <i>Exp.</i> 3.2.7 with the oblique derivative BC when the oblique vector $\vec{s}$ does not have direction of the solution gradient. . . . .	67
3.9	The $L_2(\Omega)$ -norm, the $MAX(\Gamma)$ -norm and the EOC for the <i>Exp.</i> 3.2.8 with oblique derivative BC when the oblique vector $\vec{s}$ does not have direction of the solution gradient. . . . .	68
3.10	The $L_2(\Omega)$ -norm, $MAX(\Gamma)$ -norm and the EOC for the <i>Exp.</i> 3.4.1 and <i>Exp.</i> 3.2.1 with the oblique derivative BC computed from shifted point mass source $\mathbf{x}_C = (0.5, 0.35)$ . . . . .	70
3.11	The $L_2(\Omega)$ -norm, $MAX(\Gamma)$ -norm and the EOC for the <i>Exp.</i> 3.4.2 and <i>Exp.</i> 3.2.7 when the oblique vector $\vec{s}$ does not have direction of the solution gradient. . . . .	71
3.12	The $L_2(\Omega)$ -norm, $MAX(\Gamma)$ -norm and the EOC for the <i>Exp.</i> 3.4.3 and <i>Exp.</i> 3.2.3 with the oblique derivative BC experiment with the shifted point mass source $\mathbf{x}_C = (-0.2, 0.1, 0.25)$ . . . . .	72
3.13	The $L_2(\Omega)$ -norm, $MAX(\Gamma)$ -norm and the EOC for the <i>Exp.</i> 3.4.4 and <i>Exp.</i> 3.2.8 with the 3D oblique derivative BC when the oblique vector $\vec{s}$ does not have direction of the solution gradient. . . . .	72
3.14	Earth: Statistics of residuals $T[m^2s^{-2}]$ on the bottom boundary $\Gamma$ . . . .	73
3.15	SR: The GPS/leveling test $[m]$ at 61 points in area of Slovakia. . . . .	74
4.1	The $L_2(\Omega)$ -norm, $MAX(\Gamma)$ -norm and the EOC for the <i>Exp.</i> 4.1.1. . . .	77
4.2	The $L_2(\Omega)$ -norm, $MAX(\Gamma)$ -norm and the EOC for the <i>Exp.</i> 4.1.2. . . .	78
4.3	Earth: Statistics of residuals $[m^2s^{-2}]$ between the disturbing potential obtained by solving the NFGbVP and the disturbing potential generated from EGM2008 in the global experiment. . . . .	79
4.4	SR: The GPS/levelling test $[m]$ for different NFGbVP iterations at 61 points in the area of Slovakia. . . . .	81
4.5	SR: The GPS/leveling test $[m]$ at 61 points in area of Slovakia. . . . .	81

# List of shortcuts

- ABC - Artificial Boundary Condition
- BC - Boundary Condition(s)
- Bi-CGSTAB - Biconjugate Gradient Stabilized Method
- BEM - Boundary Element Method
- EOC - Experimental Order of Convergence
- FEM - Finite Element Method
- FFT - Fast Fourier Transform
- FGBVP - Fixed Gravimetric Boundary Value Problem
- FVM - Finite Volume Method
- GBVP - Geodetic Boundary Value Problem
- GNSS - Global Navigation Satellite System
- LGBVP - Linearized Gravimetric Boundary Value Problem
- NGBVP - non-linear Geodetic Boundary Value Problem
- NUMA - Non-Uniform Memory Access
- MPI - Message Passing Interface

- PDE - Partial Differential Equation
- RMS - Root Mean Square
- SOR - Successive Over-Relaxation
- WGS84 - World Geodetic System 1984

# Introduction

The main goal of physical geodesy is the precise determination of the external gravity field of the Earth and its equipotential surface called geoid. From the mathematical point of view, the external geodetic boundary value problem (GBVP) is formulated in the form of the Laplace partial differential equation for the unknown potential in the external domain. Various boundary conditions (BCs) defined on the Earth surface are considered, e.g. the Newton BC is prescribed, if the so-called gravity anomalies are used, or the Neumann BC is prescribed, if the so-called gravity disturbances are used.

First, we will consider that the normal derivative of the unknown potential field is given on the Earth's surface, then, the oblique derivative of the unknown potential field will be considered on the Earth's surface and finally the non-linear BC for the norm of gravity potential will be studied. Recently, also a Dirichlet BC has been used in case of the GBVP solved in bounded domains. In such cases, the Neumann BC is considered on the Earth's surface and the Dirichlet BC on the other boundaries, e.g. on the sphere far from the Earth surface. The BCs on the Earth surface are given by the gravimetric measurements and the Dirichlet BCs are taken from the satellite mission (e.g. GOCE, GRACE, CHAMP) and/or from the global geopotential models (e.g. EGM2008, DNSC10-GRAV).

Nowadays, the efficiency of numerical methods like the boundary element method (BEM), the finite element method (FEM) or the finite volume method (FVM) has rapidly increased with a development of HPC (high-performance computing) facilities.

Opportunities for large scale and parallel computations make these methods applicable also for the precise global gravity field modeling. In contrary to the methods that use global basis functions like the spherical harmonics (SH), the aforementioned numerical methods allow to use basis functions with the local support like finite elements. It has an advantage that a successive refinement of the discretization is straightforward and in general improves the precision of numerical results. The price to be paid is large memory requirements.

In this work we have continued the effort initiated in [10, 14, 13] and developed new FVM schemes and treatments in physical geodesy applications. First of all, we have built a new highly efficient parallel FVM implementation for solving the GBVP with the **Neumann BC** (Chapter 2), then we present two new FVM approaches for solving the GBVP with a **direct treatment of the oblique derivative BC** (Chapter 3) and finally we deal with an iterative treatment of solving the GBVP with the **non-linear BC for the norm of gradient**.

All numerical approximations usually transform partial differential equation to a system of linear algebraic equations that must be solved. There exist various methods to solve linear systems, among which the most powerful are the so-called nonstationary methods. In [14], the Red-Black SOR method was used for parallel solution of the FVM discretization of GBVPs. This stationary method converges, but very slowly, so the resulting CPU times were enormous. In this work we use a different parallel solver, namely BiConjugate Gradient Stabilized method (Bi-CGSTAB) because in comparison with other methods, it does not need more extra memory storage and has good convergence properties for matrices given by the FVM. Such a nonstationary parallel linear solver improved CPU time significantly, e.g., in the experiment in the Himalaya region (reported in Table 2.1) the speed up (in comparison with SOR) was about 18 on the same number of processors.

The thesis is organized as follows. In Chapter 1, we give a brief description of

historical background of this problem and we present mathematical formulation of the problems which are numerically solved, namely

- (i) the non-linear GBVP for the disturbing potential,
- (ii) the GBVP for the disturbing potential with the oblique derivative BC,
- (iii) the GBVP for the disturbing potential with the Neumann BC.

The GBVP (iii), where the derivative in the oblique direction is projected onto the normal to the Earth's surface, is used for numerical experiments for local and global gravity field modeling presented in Chapter 2. In this section, together with numerical experiments, we also describe our new parallel FVM implementation and parallel solver. In Chapter 3, we present our two approaches for solving the oblique derivative GBVP (ii) together with numerical experiments. The iterative solution to the non-linear GBVP (i) for disturbing potential is presented as well as in Chapter 4. Finally thesis is ended by the conclusions.

# Chapter 1

## Formulation of the geodetic boundary value problems

### 1.1 Historical background

From the very beginning people imagined the Earth as a plate. The first man who proposed a spherical shape of the Earth was Pythagoras in the 6<sup>th</sup> century BC. Then Eratosthenes invented a system of latitude and longitude and calculated the radius of the Earth with a circumference of 46 620 *km* (error 16%). However, with the fall of the Greek empire, the scientific study declined [55].

In the Middle Ages the idea of a flatten Earth was finally rejected and new attempts were made to measure the Earth circumference. Columbus and da Gama revived the interest for the shape of the Earth. First who derived a new estimation was a French physicist Fernel in 1525 with 1% error. Development of new instruments brought other, and more accurate, techniques possible. The most important one for geodesy was the invention of the theodolite. Snellius introduced the methodology of triangulation and he determined the Earth's circumference with error of 3%. Although his result was not very accurate, he introduced a technique of measuring distance using triangulation. Newton's mechanical laws led him to the conclusion that gravity, as observed by a pendulum, must be of decreasing magnitude from the poles towards the equator due to the centrifugal force. Furthermore, he or Picard, hypothesized that the Earth is

an oblate spheroid, instead of a perfect sphere. Newton's hypothesis of an oblate spheroidal Earth was confirmed in Peru expedition in 1736. Here Bouguer recognized the effect of mountains on the deflection of vertical and the gravity.

Connection between the gravity flattening and the geometrical flattening of the ellipsoid was published in 1738 by Clairaut and it can be identified as the first step towards the solution of the GBVP. More general expression was derived by Stokes in 1849, where he considered the variation of gravity at different points on the Earth. His publication *On the variation of gravity at the surface of the Earth* [53] started a new period in the history of the knowledge of the physical Earth's shape. In this publication he proposed a solution of the GBVP for disturbing potential  $T$  (see also (1.2.21)) in the form of surface integral [53]

$$T(P) = \frac{R}{4\pi} \int_{\sigma} S(\psi) \Delta g_0 d\sigma, \quad (1.1.1)$$

where  $S(\psi)$  is the so-called Stokes function,  $\Delta g_0$  is the reduced gravity anomaly and  $\sigma$  is the geoid. Using the *Brun's formula* the disturbing potential  $T$  can be transformed to the geoidal height (geoid undulation):

$$N(Q_0) = \frac{T(P_0)}{\gamma(Q_0)}, \quad (1.1.2)$$

where  $\gamma(Q_0)$  is a normal gravity (see also (1.2.20)),  $P_0$  is defined on the geoid and  $Q_0$  on the ellipsoid, see Fig 1.1.1 a). In this way the Stokes integral connects  $\Delta g_0$ , reduced gravity anomalies, with geoidal heights  $N$  above the reference ellipsoid. The major drawback of the Stokes integral is assumption of a mass free space outside the geoid and the need for reduction of the gravity anomalies from the Earth's surface to the geoid.

In 1920, Meinesz designed a new gravimeter, which has two pendula of the same size hanging in a frame but moving in opposite phases. He had discovered that horizontal

accelerations had no influence on the difference in amplitude between the two pendula. This discovery started measuring gravity at sea.

In 1945, Molodensky published a method for the determination of the figure of the Earth and its gravity field from the surface observations of the potential and the gravity vector, free of assumptions on the density. He proposed a solution in the series of integrals [40]

$$T(P) = \sum_{n=0}^{\infty} T_n(P). \quad (1.1.3)$$

The first component of the series is formally identical with the Stokes integral (1.1.1) where only the surface gravity anomaly is used. The second component is usually approximated by the terrain corrections. Together they are called gradient solution and have form

$$T(P) = \frac{R}{4\pi} \int_{\sigma} S(\psi) [\Delta g(Q) + G_1] d\sigma, \quad (1.1.4)$$

where  $\Delta g(Q)$  is surface gravity anomaly,  $G_1$  is a terrain correction and  $\sigma$  is a telluroid, see Fig 1.1.1 b). The quasigeoidal height above the ellipsoid  $\zeta(Q)$  can be computed by *Brun's formula*

$$\zeta(Q) = \frac{T(P)}{\gamma(Q)}, \quad (1.1.5)$$

where  $P$  is on the Earth's surface and  $Q$  is defined on the telluroid.

Another solution to the Molodensky problem was defined in 1964 by Brovar [8]. He also proposed the solution in the form of series of integrals but in a simpler way by using generalized surface density and potential of a generalized surface layer. The next step forward in the theory of the GBVP, was proposed by Hörmander in 1976 [20] and improved by Sansó in 1977 [46]. They used the transformation of the problem to the gravity space, where a fixed GBVP could be obtained at the expense of a general elliptic equation. Sansó also investigated the existence and uniqueness of the solution of the linear and the non-linear GBVP. Various aspects of the non-linear GBVP are also considered e.g. in [41, 15, 19].

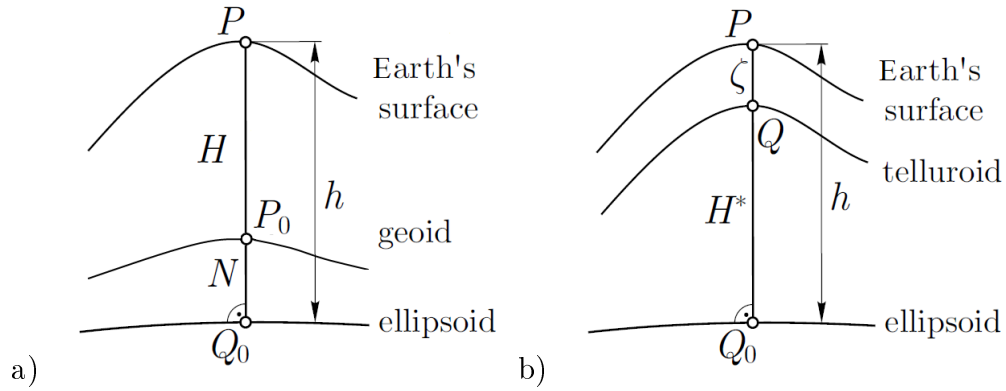


Figure 1.1.1: Illustration of the different approaches a) Stokes approach b) Molodensky approach, where  $H^*$  is the normal height,  $H$  is the orthometric height,  $h$  is the geometric height,  $\zeta$  is the height anomaly and  $N$  is the geoid undulation [54].

The problems of Stokes and Molodensky require a continuous coverage of the entire boundary of the Earth with observations. This is far from reality because measurements will always be discrete. On the other hand, new types of observations became available, such as sea surface heights from satellite altimetry. The combination of gravity and potential observations on the continents, and altimetry over ocean areas, brings new results in the altimetry-gravimetry GBVP, c.f. [21, 45].

The introduction of new kinds of observations, in addition to the classical observations as leveling, gravimetry and astronomical observations, gave an impulse for the development of overdetermined BVPs. More observations than unknowns are available; the adjustments of data is used to improve the precision of the solution, see e.g. [16, 45].

Nowadays a precise satellite positioning, such as GNSS, provides station coordinates without knowledge of the (local) gravity field. Then the so-called fixed gravimetric BVP (FGBVP), with a known 3D position of the Earth's surface, is formulated to determine the gravity field from gravimetric measurements, see [3, 19, 30].

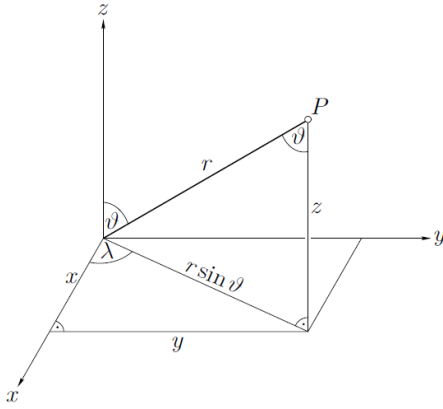


Figure 1.2.1: Rectangular and spherical coordinates [54].

## 1.2 The Earth's gravity field

We define the Cartesian coordinate system  $xyz$  in the usual way: the origin is at the Earth's center of mass, the  $z$  - *axis* coincides with the mean axis of rotation, the  $x$  - *axis* lies in the mean Greenwich meridian plane and is normal to the  $z$  - *axis*, the  $y$  - *axis* is normal to the  $xz$  - *plane*, see Fig. 1.2.1.

According to Newton's law the gravitational potential  $W_g$  may be expressed by the formula

$$W_g = W_g(\mathbf{x}) = G \int_{Earth} \frac{\rho(Q)}{r(P, Q)} dv_Q, \quad (1.2.1)$$

where  $P$  is a point having coordinates  $\mathbf{x} = (x, y, z)$ ,  $Q$  is a point variable within the Earth's body, which forms the center of the volume element  $dv_Q$ ,  $r(P, Q)$  is Euclidian distance between  $P$  and  $Q$ ,  $\rho(Q)$  is the mass density at  $Q$  and  $G$  is the gravitational constant.

The equation (1.2.1) has only a theoretical value because its practical use would require the knowledge of the detailed density distribution within the Earth which obviously is not known. For large distances  $r$  we can express (1.2.1) as

$$W_g = \frac{GM}{r}, \text{ which implies } \lim_{r \rightarrow \infty} W_g = 0, \quad (1.2.2)$$

with  $M$  denoting the total mass of the Earth's body. The physical meaning of this equation is that at large distances any body acts gravitationally as a point mass.

The gravity potential  $W$  associated with the rotating Earth is the sum of  $W_g$  and the centrifugal force

$$W_c = \frac{1}{2}\omega^2(x^2 + y^2), \quad (1.2.3)$$

so that

$$W = W_g + \frac{1}{2}\omega^2(x^2 + y^2), \quad (1.2.4)$$

where  $\omega$  is the angular velocity of the Earth's rotation.

In general, the potential  $W_g$  satisfies the *Poisson equation*, see [54],

$$\Delta W_g = -4\pi G\rho, \quad (1.2.5)$$

where  $\rho$  is a density,  $\Delta$  is the Laplace operator in the form

$$\Delta = \frac{\partial^2}{\partial x^2} + \frac{\partial^2}{\partial y^2} + \frac{\partial^2}{\partial z^2}. \quad (1.2.6)$$

Outside the attracting bodies, in the empty space, the density  $\rho = 0$  (approximately) and (1.2.5) becomes

$$\Delta W_g = 0. \quad (1.2.7)$$

This is the Laplace equation and its solutions are called harmonic functions.

Differentiating (1.2.3) yields

$$\Delta W_c = 2\omega^2, \quad (1.2.8)$$

and opposite to  $W_g$ ,  $W_c$  is not harmonic.

From (1.2.5) and (1.2.8), we obtain the equation for the gravity potential  $W$

$$\Delta W = -4\pi G\rho + 2\omega^2, \quad (1.2.9)$$

which in outer space becomes

$$\Delta W = 2\omega^2. \quad (1.2.10)$$

The *gravity vector*  $\vec{g}$  is defined as the gradient of the gravity potential, i.e.

$$\vec{g} = \nabla W, \quad (1.2.11)$$

where

$$\nabla W = \left( \frac{\partial W}{\partial x}, \frac{\partial W}{\partial y}, \frac{\partial W}{\partial z} \right)^T. \quad (1.2.12)$$

The magnitude of the gravity vector  $\vec{g}$  is called the *gravity* and is denoted by

$$g = |\nabla W|. \quad (1.2.13)$$

Direction of  $\vec{g}$ , expressed by unit a vector  $\vec{v} = g^{-1}\vec{g}$ , is the *direction of the vertical*.

The surface

$$W = \text{constant}, \quad (1.2.14)$$

on which the potential  $W$  is constant, is called the *equipotential surface* or the *level surface*. The surface of oceans, after some idealization, is a part of a certain level surface. This particular equipotential surface was proposed as the mathematical figure of the Earth and was later termed the *geoid*. The geoid is thus defined by condition

$$W = W_0 = \text{constant}. \quad (1.2.15)$$

The lines that intersect all equipotential surfaces orthogonally are not exactly straight but slightly curved, see Fig. 1.2.2, they are called *lines of force*, or *plumb lines* and they tangent corresponds to the direction of vertical.

The sphere or ellipsoid may be considered as some normal surface for the geoid. It is natural to use the external gravity potential of normal surface as a normal gravity

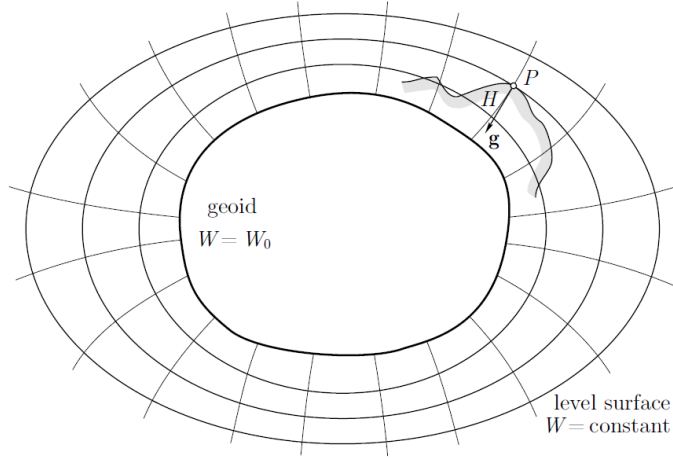


Figure 1.2.2: Level surfaces and the geoid [54].

potential  $U$  to approximate the Earth's external gravity potential  $W$ . Since geoid is an equipotential surface of  $W$ , we assume that the ellipsoid is an equipotential surface for  $U$ . Furthermore,  $U$  must be the sum

$$U = U_g + \frac{1}{2}\omega^2(x^2 + y^2), \quad (1.2.16)$$

of a normal gravitational potential  $U_g$  and a centrifugal potential, and  $U_g$  must satisfy the Laplace equation

$$\Delta U_g = 0, \quad (1.2.17)$$

outside the normal surface and behave at infinity approximately as a point mass:

$$U_g = \frac{G\bar{M}}{r}, \text{ which implies } \lim_{r \rightarrow \infty} U_g = 0, \quad (1.2.18)$$

where  $\bar{M}$  denotes the total mass enclosed by the ellipsoid. These equations correspond to (1.2.4), (1.2.7), and (1.2.2). The components of the *normal gravity vector*

$$\vec{\gamma} = \nabla U, \quad (1.2.19)$$

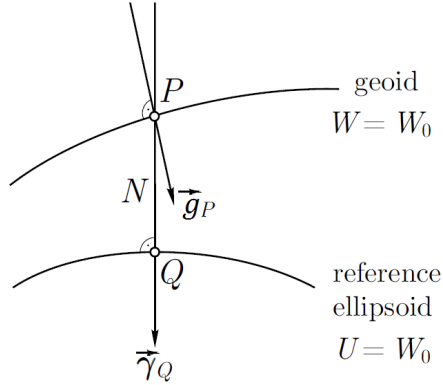


Figure 1.2.3: Geoid and reference ellipsoid [54].

as a vector to the normal surface can be easily computed, see [49], and its magnitude

$$\gamma = |\nabla U|, \quad (1.2.20)$$

is a *normal gravity*.

A difference between the actual gravity potential  $W$  and the normal gravity potential  $U$  is denoted by  $T$ , so that

$$W = U + T, \quad (1.2.21)$$

$T$  is called the *disturbing potential* or anomalous potential. If the model field is generated by a normal surface (e.g. massive ellipsoid) rotating with the Earth spin velocity  $\omega$ , its constant surface potential is equal to geopotential  $W_0$  and its mass is the same as the mass of the Earth, then the disturbing potential  $T$  outside the Earth satisfies the Laplace equation

$$\Delta T = 0. \quad (1.2.22)$$

It follows from the fact that  $T$  does not have any centrifugal component since the centrifugal component of the Earth is the same as the centrifugal component of the normal body.

Now, let us consider the gravity vector  $\vec{g}$  at point  $P$  and the normal gravity vector

$\vec{\gamma}$  at  $Q$ , see Fig. 1.2.3. The *gravity anomaly vector*  $\vec{\Delta g}$  is defined as their difference,

$$\vec{\Delta g} = \vec{g}_P - \vec{\gamma}_Q. \quad (1.2.23)$$

Vectors  $\vec{g}$  and  $\vec{\gamma}$  are characterized by magnitude and direction. The difference in magnitude is called the *gravity anomaly*

$$\Delta g = g_P - \gamma_Q. \quad (1.2.24)$$

and difference in direction is the *deflection of the vertical*. Because sphere or ellipsoid are mathematically defined we are also able to compare vectors  $\vec{g}$  and  $\vec{\gamma}$  at the same point  $P$  (e.g. on the Earth surface). Then we get the *gravity disturbance vector*

$$\vec{\delta g} = \vec{g}_P - \vec{\gamma}_P. \quad (1.2.25)$$

The difference in magnitude is the so-called *gravity disturbance*

$$\delta g = g_P - \gamma_P. \quad (1.2.26)$$

### 1.3 The geodetic boundary value problems

As we have explained in the previous section, the basic GBVP for actual gravity potential outside the Earth can be formulated in the following sense

$$\Delta W = 2\omega^2 \text{ in } \tilde{\Omega}, \quad (1.3.1)$$

$$|\nabla W| = g \text{ on } \Gamma. \quad (1.3.2)$$

where  $\tilde{\Omega}$  is the exterior space outside the Earth and  $\Gamma$  is the boundary of  $\tilde{\Omega}$  representing the Earth surface.

We note that the ultimate goal of our work is to solve this non-linear GBVP numerically. We suggest a new iterative approach for this numerical solution by subsequently solving the oblique derivative problems for which we develop an original stable and efficient finite volume schemes.

Since in geodesy we used to use the disturbing potential  $T$ , by using (1.2.21) and (1.2.22) it follows that (1.3.1)-(1.3.2) can be rewritten into the form

$$\Delta T = 0 \text{ in } \tilde{\Omega}, \quad (1.3.3)$$

$$|\nabla(T + U)| = g \text{ on } \Gamma, \quad (1.3.4)$$

Moreover, we assume that  $T$  is regular at infinity, i.e.

$$T \rightarrow 0 \text{ as } \mathbf{x} \rightarrow \infty. \quad (1.3.5)$$

One can write the norm of the gradient of the gravity potential in the form

$$|\nabla W| = \left\langle \frac{\nabla W}{|\nabla W|}, \nabla W \right\rangle, \quad (1.3.6)$$

where  $\langle, \rangle$  denotes the inner product. By inserting (1.3.6) into equation (1.3.4), we obtain

$$\left\langle \frac{\nabla(T + U)}{|\nabla(T + U)|}, \nabla(T + U) \right\rangle = g. \quad (1.3.7)$$

If we denote

$$\vec{v} = \frac{\nabla(T + U)}{|\nabla(T + U)|}, \quad (1.3.8)$$

we can rewrite the BC (1.3.4) as

$$\langle \nabla T, \vec{v} \rangle = g - \langle \nabla U, \vec{v} \rangle \text{ on } \Gamma. \quad (1.3.9)$$

Since the unit vector  $\vec{v}$ , defining the direction of the actual gravity vector, is unknown

and depends on  $T$ , the BC (1.3.9) is still non-linear, but its form allows to use an iterative approach for determining  $\vec{v}$  and  $T$  such that (1.3.3)-(1.3.5) is fulfilled. The iterative procedure for solving the GBVP (1.3.3)-(1.3.5) is defined as follows

$$\Delta T^{n+1} = 0 \text{ in } \tilde{\Omega}, \quad (1.3.10)$$

$$\langle \nabla T^{n+1}, \vec{v}^n \rangle = g - \langle \nabla U, \vec{v}^n \rangle \text{ on } \Gamma, \quad (1.3.11)$$

$$T^{n+1} \rightarrow 0 \text{ as } \mathbf{x} \rightarrow \infty, \quad (1.3.12)$$

for  $n = 0, 1, 2, \dots$ , where

$$\vec{v}^n = \frac{\nabla(T^n + U)}{|\nabla(T^n + U)|}, \quad (1.3.13)$$

and we start the iterations by choosing  $T^0 = 0$ , i.e.  $W^0 = U$  and correspondingly for  $\vec{v}^0$  we get

$$\vec{v}^0 = \frac{\nabla U}{|\nabla U|} = \vec{s}, \quad (1.3.14)$$

where  $\vec{s}$  represents the unit vector in direction of the normal gravity vector. One can see that in every iteration we solve the GBVP for  $T^{n+1}$  with prescribed oblique derivative vector  $\vec{v}^n$ .

It is worth to note that in the first step ( $n = 0$ ) the problem (1.3.11)-(1.3.12) represents the so-called linearized FGBVP [30, 22, 23, 10, 13] with the oblique derivative BC given by

$$\langle \nabla T^1, \vec{s} \rangle = g - \gamma = \delta g. \quad (1.3.15)$$

In further iterations we improve the direction of the unit vector  $\vec{v}$  by which we reduce the linearization error implicitly included in definition of the FGBVP.

So the classical FGBVP with the oblique derivative BC is written in this form

$$\Delta T = 0 \text{ in } \tilde{\Omega}, \quad (1.3.16)$$

$$\langle \nabla T, \vec{s} \rangle = \delta g \text{ on } \Gamma, \quad (1.3.17)$$

$$T \rightarrow 0 \text{ as } \mathbf{x} \rightarrow \infty. \quad (1.3.18)$$

The FGBVP (1.3.16)-(1.3.18) is defined in the infinite domain  $\tilde{\Omega}$ . For our further purposes we construct a bounded domain  $\Omega \subset \tilde{\Omega}$ , see Fig. 1.3.1. In order to construct domain  $\Omega$  we use a methodology of the artificial boundary method (ABM) [18]. The main idea of the artificial boundary method is to construct a "suitable" artificial boundary condition (ABC) on the artificial boundary satisfied by the solution of the original problem exactly or approximately, and then reduce the original problem to a BVP on a bounded computational domain. The suitable ABC satisfies the following basic requirements [18]:

- The reduced problem is well-posed, i.e., the reduced problem has a unique solution and the solution depends continuously on the boundary data.
- Restricted to the bounded computational domain, the solution of the reduced problem is the same as the solution of the original problem, or it is a good approximation of the solution of the original problem (our case).
- The bounded computational domain should be as small as possible, in order to reduce the computational work and memory requirement.
- The reduced problem on the bounded computational domain should be easily solved numerically.

Now we introduce an artificial boundary, for example  $\Gamma_R = \{\mathbf{x}, |\mathbf{x}| = R\}$  where  $R > 0$  is a real number, and  $\Gamma_R \subset \tilde{\Omega}$ . For 2D problems,  $\Gamma_R$  is a circle with radius  $R$ , and for 3D problems,  $\Gamma_R$  is a sphere.

The artificial boundary  $\Gamma_R$  divides  $\tilde{\Omega}$  into two parts, the unbounded part  $\Omega_{ext} = \{\mathbf{x}, |\mathbf{x}| > R\}$  and the bounded part  $\Omega = \tilde{\Omega} \setminus \Omega_{ext}$ . The computational domain  $\Omega$  has the boundary  $\partial\Omega = \Gamma \cup \Gamma_R$ . For the problem (1.3.16)-(1.3.18), if we can find an exact boundary condition or good approximation on  $\Gamma_R$  for the unknown  $T$ , then we can reduce the given problem on unbounded domain to a problem on the bounded computational domain  $\Omega$ , and find the numerical solution on  $\Omega$ .

A first idea for choosing ABC is to shift the condition (1.3.18) at infinity to the artificial boundary  $\Gamma_R$

$$T = 0 \text{ on } \Gamma_R, \quad (1.3.19)$$

The question is whether the solution of the reduced problem is a good approximation of  $T$  on the domain  $\Omega$ . We can see from the following example that solution in bounded domain is only a rough approximation of  $T$  on  $\tilde{\Omega}$ .

Let  $\Gamma = \{\mathbf{x}, |\mathbf{x}| = 1\}$ ,  $\delta g = 1$  and  $\vec{s}$  be a unit outward normal in problem (1.3.16)-(1.3.18). The error between the solution in an unbounded and bounded domain can be expressed as

$$error = \frac{1}{R}, \quad (1.3.20)$$

where  $R > 1$ . From this example, we see that for the simple BC (1.3.19) accuracy of the solution of the reduced problem depends on the position of the artificial boundary. The position of the artificial boundary must be far away from the origin, in order to get a high accuracy, i.e., the computational domain should be very large, which implies a large computational time and storage requirement.

Another idea for ABC is setting

$$T = \mu \text{ on } \Gamma_R, \quad (1.3.21)$$

where  $\mu$  is a good approximation of the solution on  $\Gamma_R$ .

In this case, the error solution in unbounded and bounded domain we can express

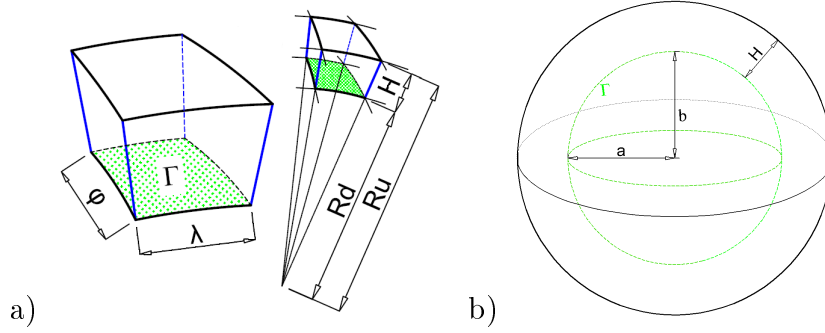


Figure 1.3.1: Plots of the bounded domain  $\Omega$ : a) local, b) global case. The part of the boundary  $\Gamma$  represents the Earth surface and is plotted in green. Artificial boundaries are plotted in black (upper spherical part) and in blue (planar sides of the domain in case a).

as

$$error = \frac{1}{R} - \mu. \quad (1.3.22)$$

From this example, we see that for the BC (1.3.21), the accuracy of the solution of the reduced problem depends on the position of the artificial boundary reduced by value  $\mu$ . The position of the artificial boundary does not need to be far away from the origin, when the value  $\mu$  is a good approximation of the solution on  $\Gamma_R$ .

Now, we are able to rewrite problem (1.3.16)-(1.3.18) to the bounded domain  $\Omega$ . Thus, we will consider the following modified-FGBVP:

$$\Delta T = 0 \text{ in } \Omega, \quad (1.3.23)$$

$$\langle \nabla T, \vec{s} \rangle = \delta g \text{ on } \Gamma, \quad (1.3.24)$$

$$T = T_{SAT} \text{ on } \partial\Omega - \Gamma, \quad (1.3.25)$$

where  $T_{SAT}$  represents the disturbing potential generated from the satellite-only geopotential model. We assume that data measured by satellites on their orbits gives good approximation of actual disturbing potential.

The boundary condition (1.3.24) represents the oblique derivative BC included in the original FGBVP formulation. We will also use the simplified model where we

project the oblique derivative into the normal to the boundary  $\Gamma$  [10, 13]. So for the normal derivative we use approximation  $\frac{\partial T}{\partial n_\Gamma} = \delta g(\mathbf{x}) \cdot \cos \mu(\mathbf{x}) = \delta g^*(\mathbf{x})$ , where  $\mu(\mathbf{x}) = \angle(\vec{s}, \vec{n}_\Gamma)$  is the angle between  $\vec{s}$  and  $\vec{n}_\Gamma$ ,  $\vec{n}_\Gamma$  is a unit outward normal vector to  $\Gamma$ . It is worth to note that new quantity  $\delta g^*(\mathbf{x})$  represents the projection of the vector  $\delta g(\mathbf{x})\vec{s}(\mathbf{x})$  to the normal  $n_\Gamma$  and not a projection of the gradient  $\nabla T$  onto this normal.

With this approximation we solve the following Neumann-FGBVP:

$$\Delta T = 0 \text{ in } \Omega, \quad (1.3.26)$$

$$\frac{\partial T}{\partial n_\Gamma} = \delta g^* \text{ on } \Gamma, \quad (1.3.27)$$

$$T = T_{SAT} \text{ on } \partial\Omega - \Gamma. \quad (1.3.28)$$

In the following chapters we will subsequently present numerical methods for solving problems (1.3.26)-(1.3.28), (1.3.23)-(1.3.25) and finally the numerical solution of the non-linear FGBVP (NFGBVP) defined in the bounded domain, i.e.

$$\Delta T = 0 \text{ in } \Omega, \quad (1.3.29)$$

$$|\nabla(T + U)| = g \text{ on } \Gamma, \quad (1.3.30)$$

$$T = T_{SAT} \text{ on } \partial\Omega - \Gamma. \quad (1.3.31)$$

## 1.4 Numerical approaches for solving GBVP

There exist various numerical approaches to solve such potential problems. The spherical harmonics based methods are used for the global gravity field modelling, c.f. [37, 43], and on the other hand, the fast Fourier transformation (FFT) methods (e.g. [51]) and least-squares collocation (e.g. [48]) are often used in case of the remove-compute-restore (RCR) technique for the local gravity field modelling.

However, a recent development of computing facilities has brought new opportunities in numerical solution to the boundary value problems in physical geodesy. Numerical methods like the boundary element method, the finite element method, the finite difference method, the finite volume method and others have been applied for gravity field modelling. The BEM was innovatively applied by Klees in [26]. This approach based on the Galerkin BEM and the indirect BEM formulation was later extended [27, 28] and parallel computing [31, 32, 33] and fast multipole method were efficiently implemented [29]. Later Čunderlík et al. [9, 10, 11] presented the direct BEM formulation based on the collocation method for solving the linearized fixed gravimetric BVP. In case of the FEM, the pioneering work has been done by Meissl [38] and Shaofeng and Dingbo [52]. Later, the finite element technique for the solution of gravimetric BVPs with mixed BCs in 3D domains above the Earth's surface was studied by Fašková et al. in [13, 14]. The FDM was applied by Keller in [25]. Other numerical approaches based on a weak formulation of the BVP and minimization of a quadratic functional were developed in Holota [23], Holota and Nesvadba [24], and Nesvadba et al. [42]. Recently, the FVM was applied by Fašková in [14] and we have continued a development of the FVM for geodetic applications in this thesis.

# Chapter 2

## Numerical solution of the Neumann boundary-value problem

### 2.1 The finite volume method

To solve (1.3.26)-(1.3.28), we have chosen the finite volume method (FVM), [12]. In FVM we divide the computational domain  $\Omega$  into finite volumes  $p$ , multiply the Laplace equation by minus one (for positive operator) and integrate the resulting equation over each finite volume with a use of the divergence theorem that turns the volume integral into the surface integral,

$$-\int_p \Delta T \, dx dy dz = -\int_{\partial p} \nabla T \cdot \vec{n} \, d\sigma, \quad (2.1.1)$$

from where we get

$$-\int_{\partial p} \frac{\partial T}{\partial n} d\sigma = 0. \quad (2.1.2)$$

in the finite volume  $p$ . Let  $q \in N(p)$  be a neighbour of the finite volume  $p$ , where  $N(p)$  denotes all neighbours of  $p$ . Let  $T_p$  and  $T_q$  be approximate values of  $T$  in  $p$  and  $q$ ,  $e_{pq}$  be a boundary of the finite volume  $p$  common with  $q$ ,  $\vec{n}_{pq}$  be its unit normal vector oriented from  $p$  to  $q$ ,  $m(e_{pq})$  is the area of  $e_{pq}$ . Let  $x_p$  and  $x_q$  be representative points of  $p$  and  $q$  respectively and  $d_{pq}$  their distance. If we approximate the normal derivative

along the boundary of volume  $p$  by

$$\frac{\partial T}{\partial n_{pq}} \approx \frac{T_q - T_p}{d_{pq}}, \quad (2.1.3)$$

we obtain from (2.1.3)

$$-\sum_{q \in N_p} \frac{T_q - T_p}{d_{pq}} m(e_{pq}) = \sum_{q \in N_p} \frac{m(e_{pq})}{d_{pq}} (T_p - T_q) = 0, \quad (2.1.4)$$

which represents the linear system of algebraic equations for the FVM. Then the term  $\frac{m(e_{pq})}{d_{pq}}$  defined on sides of the finite volume  $p$  is referred to as the transmissivity coefficient [12].

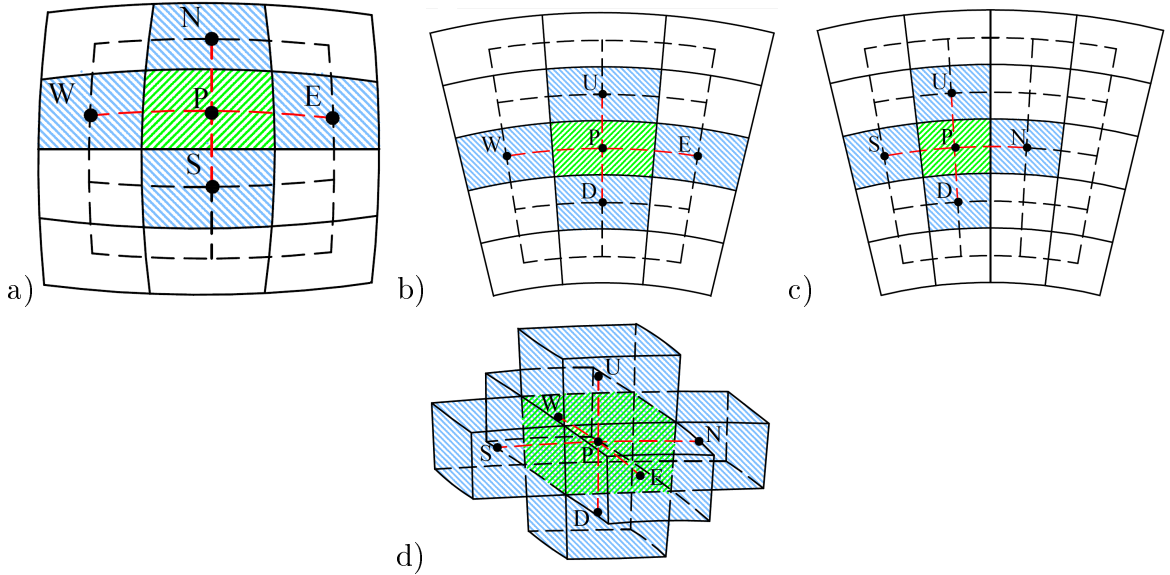


Figure 2.1.1: Illustration of the grid ( $n_1 = 3, n_2 = 4, n_3 = 5$ ). a) Horizontal cut b) Vertical cut in zonal direction c) Vertical cut in meridional direction d) 3D view. The volume  $p$  is hatched by dots, while its adjacent volumes  $q$  are hatched by dashed lines.

The system (2.1.4) must be accompanied by the boundary conditions. In case of the Neumann BC (1.3.28) we prescribe the value for the term on the right-hand side of (2.1.3) on the boundary and in case of the Dirichlet BC we prescribe the value of  $T_q$  on the boundary. In case of the oblique derivative BC on bottom boundary (1.3.24) it needs a special treatment which will be discussed in Chapter 3.

### 2.1.1 Transmissivity coefficients for spherical domains

Now we restrict our considerations to the specific situation depicted in Figure 2.1.1. We define indices  $i = 1, \dots, n_1, j = 1, \dots, n_2$  and  $k = 1, \dots, n_3$  in the direction of the longitude  $\lambda$ , latitude  $\varphi$  and radius  $R$ .

The length of segments in spherical coordinates are equal to  $\tilde{d}\lambda = \frac{\lambda_u - \lambda_d}{n_1}$ ,  $\tilde{d}\varphi = \frac{\varphi_u - \varphi_d}{n_2}$ ,  $dR = \frac{R_u - R_d}{n_3}$ , where  $\lambda_u, \varphi_u$  and  $R_u$  denote the upper boundary of the range of longitude, latitude and radius,  $\lambda_d, \varphi_d$  and  $R_d$  their lower boundaries. Since  $d\lambda$  and  $d\varphi$  are given in spherical coordinates, we must transform them into their real lengths. If we denote by  $\lambda_{i,j,k}$  and  $\varphi_{i,j,k}$  the values of  $\lambda$  and  $\varphi$  in point  $x_p = x_{i,j,k}$ , we obtain the lengths

$$d\lambda_{i,j,k} = (R_d + kdR)\tilde{d}\lambda \cos(\varphi_{i,j,k}), \quad (2.1.5)$$

$$d\varphi_{i,j,k} = (R_d + kdR)\tilde{d}\varphi. \quad (2.1.6)$$

The values on boundaries of the finite volume  $p$  are then given by  $d\lambda_{i,j \pm \frac{1}{2}, k}$ ,  $d\varphi_{i \pm \frac{1}{2}, j, k}$  and  $d\lambda_{i,j,k \pm \frac{1}{2}}$ ,  $d\varphi_{i,j,k \pm \frac{1}{2}}$ . Then the transmissivity coefficients for the finite volume  $p = (i, j, k)$  on the "west, east, north, south, up" and "down" sides are defined as follows

$$\begin{aligned} W_{i,j,k} &= \frac{d\varphi_{i-\frac{1}{2},j,k}dR}{d\lambda_{i,j,k}}, & E_{i,j,k} &= \frac{d\varphi_{i+\frac{1}{2},j,k}dR}{d\lambda_{i,j,k}} \\ S_{i,j,k} &= \frac{d\lambda_{i,j-\frac{1}{2},k}dR}{d\varphi_{i,j,k}}, & N_{i,j,k} &= \frac{d\lambda_{i,j+\frac{1}{2},k}dR}{d\varphi_{i,j,k}} \\ D_{i,j,k} &= \frac{d\varphi_{i,j,k-\frac{1}{2}}d\lambda_{i,j,k-\frac{1}{2}}}{dR}, & U_{i,j,k} &= \frac{d\varphi_{i,j,k+\frac{1}{2}}d\lambda_{i,j,k+\frac{1}{2}}}{dR}. \end{aligned} \quad (2.1.7)$$

Since the diagonal coefficient is given by

$$P_{i,j,k} = W_{i,j,k} + E_{i,j,k} + N_{i,j,k} + S_{i,j,k} + U_{i,j,k} + D_{i,j,k}, \quad (2.1.8)$$

in every inner finite volume, the linear system has the form

$$\begin{aligned}
P_{i,j,k}T_{i,j,k} - W_{i,j,k}T_{i-1,j,k} - E_{i,j,k}T_{i+1,j,k} - N_{i,j,k}T_{i,j+1,k} \\
-S_{i,j,k}T_{i,j-1,k} - U_{i,j,k}T_{i,j,k+1} - D_{i,j,k}T_{i,j,k-1} = 0.
\end{aligned} \tag{2.1.9}$$

### 2.1.2 Transmissivity coefficients for ellipsoidal domains

As a reference ellipsoid we have chosen the world geodetic system WGS84. The WGS84 surface is a biaxial ellipsoid with the major axis  $a = 6378137.0 m$  at the equator and with the flattening  $f = 1/298.257223563$ . The polar minor axis  $b$  can be computed as  $b = a(1 - f)$ , i.e.  $b = 6356752.3142 m$ . From  $a$  and  $b$  it is possible to derive the second eccentricity squared  $e^2$  of the ellipsoid in the form  $e^2 = (a^2 - b^2)/b^2$ . For the ellipsoidal domains we denote the ellipsoidal longitude by  $L$ , the latitude by  $B$  and the height by  $H$  and length of the segments in ellipsoidal coordinates are  $d\tilde{L} = \frac{L_u - L_d}{n_1}$ ,  $d\tilde{B} = \frac{(B_u - B_d)}{n_2}$ , and  $dH = \frac{H_u}{n_3}$  ( $H_d=0$ ).

In case of transmissivity coefficients for an ellipsoid, we have to compute the radii of the curvature  $M$  and  $N$  for the finite volume  $p = (i, j, k)$  by

$$M_{i,j,k} = a(1 - e^2)/(1 - e^2 \sin^2(B_d + jdB))^{3/2}, \tag{2.1.10}$$

$$N_{i,j,k} = a/\sqrt{(1 - e^2 \sin^2(B_d + jdB))}, \tag{2.1.11}$$

and the lengths of the elliptical arcs are then given by

$$dL_{i,j,k} = (kdH + N_{i,j,k}) \cos(B_d + jdB)d\tilde{L}, \tag{2.1.12}$$

$$dB_{i,j,k} = (kdH + M_{i,j,k})d\tilde{B}. \tag{2.1.13}$$

Then the transmissivity coefficients for the finite volume  $p = (i, j, k)$  on the "west, east,

north, south, up" and "down" sides of the ellipsoidal domain are defined as follows

$$\begin{aligned}
W_{i,j,k} &= \frac{dB_{i-\frac{1}{2},j,k}dH}{dL_{i,j,k}}, & E_{i,j,k} &= \frac{dB_{i+\frac{1}{2},j,k}dH}{dL_{i,j,k}} \\
S_{i,j,k} &= \frac{dL_{i,j-\frac{1}{2},k}dH}{dB_{i,j,k}}, & N_{i,j,k} &= \frac{dL_{i,j+\frac{1}{2},k}dH}{dB_{i,j,k}} \\
D_{i,j,k} &= \frac{dB_{i,j,k-\frac{1}{2}}dL_{i,j,k-\frac{1}{2}}}{dH}, & U_{i,j,k} &= \frac{dB_{i,j,k+\frac{1}{2}}dL_{i,j,k+\frac{1}{2}}}{dH}, \\
P_{i,j,k} &= W_{i,j,k} + E_{i,j,k} + N_{i,j,k} + S_{i,j,k} + U_{i,j,k} + D_{i,j,k}.
\end{aligned} \tag{2.1.14}$$

Finally, with these definitions of coefficients we have to solve the linear system of equations in the form

$$\begin{aligned}
P_{i,j,k}T_{i,j,k} - W_{i,j,k}T_{i-1,j,k} - E_{i,j,k}T_{i+1,j,k} - N_{i,j,k}T_{i,j+1,k} \\
-S_{i,j,k}T_{i,j-1,k} - U_{i,j,k}T_{i,j,k+1} - D_{i,j,k}T_{i,j,k-1} = 0.
\end{aligned} \tag{2.1.15}$$

### 2.1.3 Iterative solvers

The term "*iterative method*" refers to a wide range of techniques that use successive approximations to obtain more accurate solutions to a linear system at each iteration step. The linear system of algebraic equations, either (2.1.10) or (2.1.15), is written in the form

$$Ax = b, \tag{2.1.16}$$

where  $A$  is the matrix with given coefficients, either (2.1.8)-(2.1.10) or (2.1.8)-(2.1.15),  $b$  is the right-hand side vector and  $x$  is an unknown vector. Stationary iterative methods like the Gauss-Seidel or SOR (Successive-Over Relaxation) are easy to implement, but usually not so efficient for solving elliptic problems [14]. We use and present the nonstationary methods that are based on the idea of sequences of orthogonal vectors.

Nonstationary methods differ from stationary ones by the fact that the computations

Solver	CPU time	Number of iterations
SOR	1.107237e+05 secs	70000
Bi-CGSTAB	5.862395e+03 secs	1300

Table 2.1: Efficiency comparison of the stationary and nonstationary methods in the experiment with size  $n_1 \times n_2 \times n_3 = 500 \times 300 \times 100$ , tested on one processor.

involve information that changes in each iteration. Typically, constants are computed by taking inner products of residuals or other vectors arising in the iterative procedure. The conjugate gradient method (CG) derives its name from the fact that it generates a sequence of conjugate (or orthogonal) vectors. These vectors are the residuals of the iterates. They are also gradients of a quadratic functional, the minimization of which is equivalent to solving the linear system. Conjugate gradient method is an extremely efficient method when the coefficient matrix is symmetric positive definite since the storage for only a limited number of vectors is required. The Generalized Minimal Residual method (GMRES), developed by Saad and Schultz in 1986 [44], approximates the solution by the vector in a Krylov subspace with minimal residual. Like other iterative methods, GMRES is usually combined with a preconditioning in order to speed up convergence.

Computation costs						
Method	MV	XPY	DOT	Memory	Iter	Time
Bi-CG	2	6.5	2	7	1123	1203s
Bi-CGSTAB	1	3	2	7	567	691s
BiCGstab2	1	5.5	2.27	10	648	833s
BiCGstab(l)	1	0.75(1+3)	0.25(1+7)	2l+5	446	902s (l=4)

Table 2.2: The average memory and time costs for various BiCG linear solvers, where APXY is a number of vector scalar products, DOT is a number of scalar-vector multiplications, MEM represents a number of additional vectors needed in iterative procedure, ITER gives a number of iterations to reach the prescribed residual and TIME presents the overall CPU time in seconds. The table is constructed for a particular non-symmetric matrix from our finite volume method, and from MEM and TIME columns one can see optimality of Bi-CGSTAB. BiCGstab( $l$ ) denotes Bi-CGSTAB restarted at each  $l^{th}$  step [47].

In our approach, we have chosen the Bi-CGSTAB method [50], which is the robust and stable method developed for solving nonsymmetric linear systems of equations. In comparison with other methods, it does not need more extra memory storage and has good convergence properties for the FVM matrices arising in our application, see Table 2.1. It is also worth to note that the Bi-CGSTAB method has the lowest CPU time as well as memory requirement among all Bi-CG methods in case of our application, see Table 2.2.

The pseudocode of Bi-CGSTAB is as follows [4]:

```

Choose  $x_0, \tilde{r}_0$  and compute  $r_0 := b - Ax_0$ , put  $\tilde{r} := r^{(0)}$ 
for  $i = 1, 2, \dots$ 
   $\rho_{i-1} = (\tilde{r}, r^{(i-1)})$ 
  if  $\rho_{i-1} = 0$  method fails
  if  $i = 0$     $p^{(i)} = r^{(i-1)}$ 
  else
     $\beta_{i-1} = (\rho_i \rho_{i-1}) / (\alpha_{i-1} \omega_{i-1})$ 
     $p^{(i)} = r^{(i-1)} + \beta_{i-1}(p^{(i-1)} - \omega_{i-1}v^{(i-1)})$ 
  endif
   $v^{(i)} = Ap^{(i)}$ 
   $\alpha_i = \rho_{i-1} / (\tilde{r}, v^{(i)})$ 
   $s = r^{(i-1)} - \alpha_i v^{(i)}$ 
  check norm of  $s$ ; if small enough: set  $x^{(i)} = x^{(i-1)} + \alpha_i p$  and stop
   $t = As$ 
   $\omega_i = (t, s) / (t, t)$ 
   $x^{(i)} = x^{(i-1)} + \alpha_i p + \omega_i s$ 
   $r^{(i)} = s - \omega_i t$ 
  check convergence; continue if necessary
end

```

### 2.1.4 Parallelization of the method

Nowadays, the speed up of numerical algorithms is performed by distribution of computations into several processes using so-called Massively Parallel Processors (MPP) architecture together with the Message Passing Interface (MPI) programming framework.

The architecture of parallel computers is classified according to memory (centralized and distributed) and according to the address space (shared and individual address space). The MPP architecture uses the distributed memory together with the individual address space, i.e., each node has its own processor, memory, Input/Output subsystem and operating system. These nodes are connected by the high-speed network in order to transmit data between parallel processes and to access data that other processes have updated (message passing).

In our application we use the Single Program Multiple Data (SPMD) model, where only one program is built to run on each process and working with different part of data sets. Each process has its own unique integer identifier assigned by the system when the process initializes. The communication between processors is managed by the MPI

Size of experiment	Radial split	Meridian split
4200x2400x120	576.78	16.47
790x300x100	13.56	1.71

Table 2.3: Comparison of communication memory cost (in MB) for different data splitting in two numerical experiments.

functions. In this approach, it is important from the communication time point of view that the parallel process runs on a fixed processor during the whole computation. This can be done using the NUMA library. Further NUMA property is that it allocates a memory with the fastest access to each processor. Utilization of NUMA functions can reduce the computational time by 50 percents.

There exist several possibilities of data management in parallel implementations, see [2]. In our parallel algorithm we split all the multidimensional arrays into sections which can be allocated in the memory of single processor (max. 8 GB). In order to solve the linear system iteratively, we have created the overlapping 2D slices which are used for the exchange of information, see Figure 2.1.2 for splitting in radial direction (case *a*) and in meridional direction (case *b*). A natural splitting is given by case *a*

and used in [14]. However, in large scale numerical experiments presented in this work, it was necessary to switch to case b), because 2D slices which must be communicated have much smaller dimensions in meridian then in radial splitting. Table 2.3 reports large differences in communicated memory when using different type of splitting. This difference in communication costs results for large scale experiments in the overall speed up about 3.

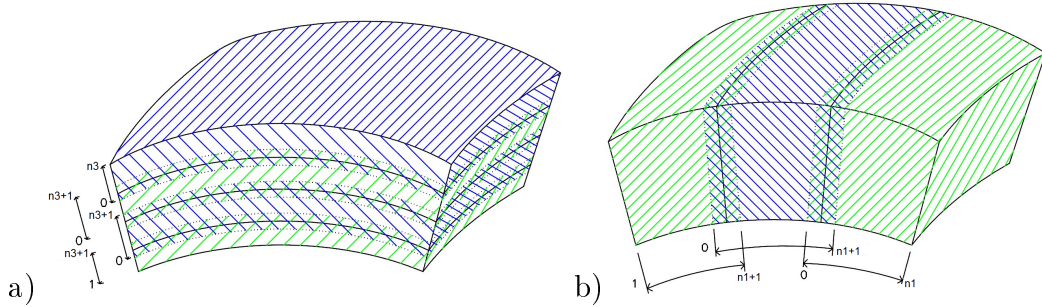


Figure 2.1.2: Different types for data splitting and overlapping over parallel processes. a) Radial split of domain b) Meridional split of domain.

## 2.2 Numerical experiments

In this section we present numerical experiments where we solve the FGBVP (1.3.26)-(1.3.28) by the FVM discussed above. The *Experiment 2.2.1* test experimental order of convergence (EOC). Comparison spherical and ellipsoidal earth approximation was done in *Experiment 2.2.3*. Finally we deal with global and local gravity field modeling.

For computing residuals we consider either the disturbing potential  $T$  or the height of quasigeoid  $\zeta$  defined by (1.1.5).

In numerical experiments, we present statistical characteristics of residuals, namely:

- the mean value =  $\overline{res} = \frac{1}{n} \sum_{p=1}^n res_p$ , where  $n = n_1 n_2$ , or  $n = n_1 n_2 n_3$
- the standard deviation =  $\sqrt{\frac{1}{n} \sum_{p=1}^n (res_p - \overline{res})^2}$ ,
- the root mean square =  $\sqrt{\frac{1}{n} \sum_{p=1}^n res_p^2} = \|res_p\|_{L_2}$ ,

where residuals are defined as a difference between our numerical and the exact (or

EGM2008) solution.

Then  $res_p = T_p - T_p^*$  or  $res_p = \zeta_p - \zeta_p^*$ , where  $T_p^*$  and  $\zeta_p^*$  is either exact or EGM2008 value in a representative point of the finite volume  $p$ . For the the numerical experiments we choose exact solution in form  $T^* = 1/r$  where  $r$  is the radius. Now we can easily compute the Dirichlet and the Neumann BCs.

### 2.2.1 Theoretical numerical experiments and experimental order of convergence

**Experiment 2.2.1.** To study the EOC, we choose the computational domain  $\Omega$  bounded domain by two spheres (Fig. 1.3.1 b)) with radii  $R_d = 1 m$  and  $R_u = 2 m$ . There has been the Neumann BC on bottom boundary applied and the Dirichlet BC on the upper spherical boundary was considered. Due to joining of meridians in the South and North Pole, the rows of finite volumes closest to the poles had only triangular base. We solve this situation by defining zero transmissivity coefficients  $S_{i,j,k} = 0$  in case of South Pole, and  $N_{i,j,k} = 0$  in case of North Pole. Comparisons of FVM solutions with the exact solution for several successive refinements can be found in Table 2.4.

$n_1 \times n_2 \times n_3$	$\ T^* - T\ _{L_2(\Omega)}$	EOC
$45 \times 22 \times 5$	0.001281	-
$90 \times 45 \times 10$	0.000285	2.16
$180 \times 90 \times 20$	0.000071	2.00
$360 \times 180 \times 40$	0.000018	1.99
$720 \times 360 \times 80$	0.000004	2.02

Table 2.4: The  $L_2(\Omega)$ -norm and the EOC of differences between the exact solution  $T^*$  and FVM solutions  $T$  for the *Exp.* 2.2.1 with Neumann BC in a domain between two spheres.

**Experiment 2.2.2.** Then in second EOC experiment we have reduced the computational domain  $\Omega$  from the previous experiment to a tesseroid (Fig. 1.3.1 a)), i.e., spherical radii have been the same  $R_d = 1 m$  and  $R_u = 2 m$ , but the spherical longitude

$\lambda$  and spherical latitude  $\varphi$  have been between  $\langle 0, 50 \rangle^\circ$ . Additionally to the previously described BCs, on the arisen side boundaries the Dirichlet BC according to the chosen exact solution has been taking into account. Results are presented in Table 2.5. One can see that the FVM approach on such domain is second order accurate as well.

$n_1 \times n_2 \times n_3$	$\ T^* - T\ _{L_2(\Omega)}$	EOC
$6 \times 6 \times 6$	0.0001698	-
$12 \times 12 \times 12$	0.0000409	2.05
$24 \times 24 \times 24$	0.0000098	2.06
$48 \times 48 \times 48$	0.0000023	2.04
$96 \times 96 \times 96$	0.0000005	2.00

Table 2.5: The  $L_2(\Omega)$ -norm and the EOC of differences between the exact solution  $T^*$  and FVM solutions  $T$  for the *Exp.* 2.2.2 with Neumann BC in a tesseroidal domain.

## 2.2.2 Comparison of FVM solutions using spherical and ellipsoidal Earth's approximation

In the following experiment we present a comparison of FVM solutions using spherical and ellipsoidal Earth's approximation.

**Experiment 2.2.3.** The numerical experiment on the sphere, deals with the computational domain  $\Omega$  bounded by the bottom spherical boundary  $\Gamma$  with radius  $6378 \text{ km}$  and the upper spherical boundary with radius  $6618 \text{ km}$  corresponding to  $\Delta R = 240 \text{ km}$ . A range for spherical latitude and longitude has been  $\varphi \in \langle 20.0^\circ, 50.0^\circ \rangle$  and  $\lambda \in \langle 60.0^\circ, 110.0^\circ \rangle$ , respectively. For the numerical experiment on an ellipsoid we have chosen the reference ellipsoid WGS84 as bottom boundary  $\Gamma$ , we have chosen the same range of ellipsoidal longitude  $L$  and latitude  $B$  as of spherical longitude  $\lambda$  and latitude  $\varphi$  and the upper ellipsoidal boundary has been at altitude  $240 \text{ km}$  above the WGS84.

The number of finite volumes in both experiments has been 1200 in radial (or height's), 900 in meridional and 1500 in zonal directions, i.e.,  $5' \times 5' \times 200 \text{ m}$  sized

volumes have been created. The gravity disturbances transformed from the free-air gravity anomalies interpolated from the DTU10-GRAV dataset [1] are prescribed on the bottom boundary. The disturbing potential on sides and upper boundary has been computed from the GOCO03S satellite only geopotential model up to degree 250 [37] that was created from: GOCE, GRACE, CHAMP and SLR data. Every computation took approximately 7.5 hours on 60 processors using 220GB of RAM.

Statistics for $\text{res} = T(\text{FVM}) - T(\text{EGM2008})$			
Domain	Mean value	St. deviation	Root mean Square
Sphere	-0.256	3.890	3.899
Ellipsoid	-0.708	0.754	1.035

Table 2.6: Himalayas: Comparison of statistical characteristics for spherical and ellipsoidal domains [ $m^2s^{-2}$ ].

Statistical characteristics of the residuals between computations on spherical as well as ellipsoidal domain and the disturbing potential generated from EGM2008 [43] are shown in Table 2.6. The visual comparisons are presented in Figure 2.2.1. As we can see, the standard deviation of residuals is significantly smaller on ellipsoidal domain than on spherical one. In Figure 2.2.1 we can observe that the differences of results obtained by the FVM on the ellipsoidal domain are much smoother in the whole region, while in the Tibetan plateau the FVM solution is  $2m^2s^{-2}$  below EGM2008. On spherical domain the differences have much higher variability which leads us to the conclusion that usage of ellipsoidal computational domain is more appropriate for our FVM solution of Neumann-FGBVP.

### 2.2.3 Global and local gravity field modelling

With respect to results obtained in the previous *Experiment 2.2.3*, in all following experiment we deal only with the ellipsoidal computational domain and we present one global and local numerical numerical solution using real data.

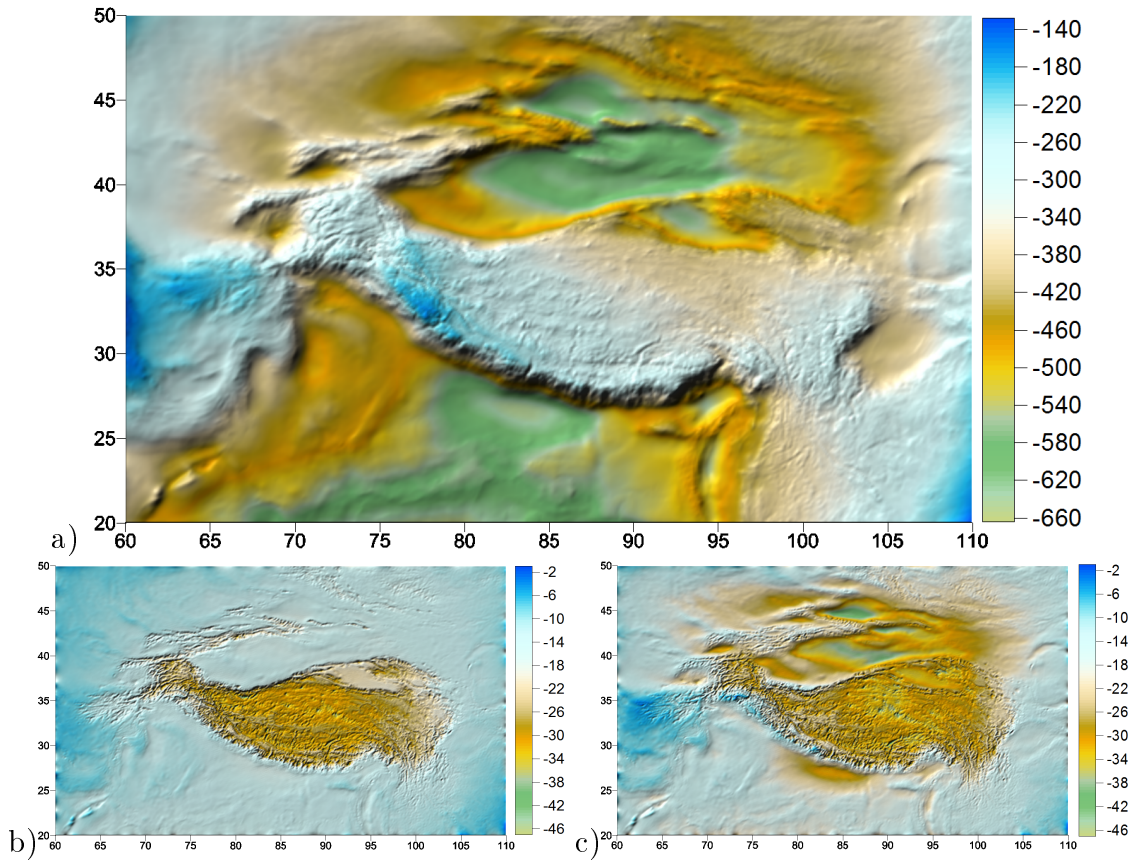


Figure 2.2.1: Himalayas: a) The disturbing potential solution  $T[m^2.s^{-2}]$  above Himalayas computed by the FVM. b) residuals  $T[m^2.s^{-2}]$  between the ellipsoidal FVM solution and the disturbing potential generated directly from EGM2008 on the bottom boundary  $\Gamma$ . c) residuals  $T[m^2.s^{-2}]$  between the spherical FVM solution and EGM2008 solution.

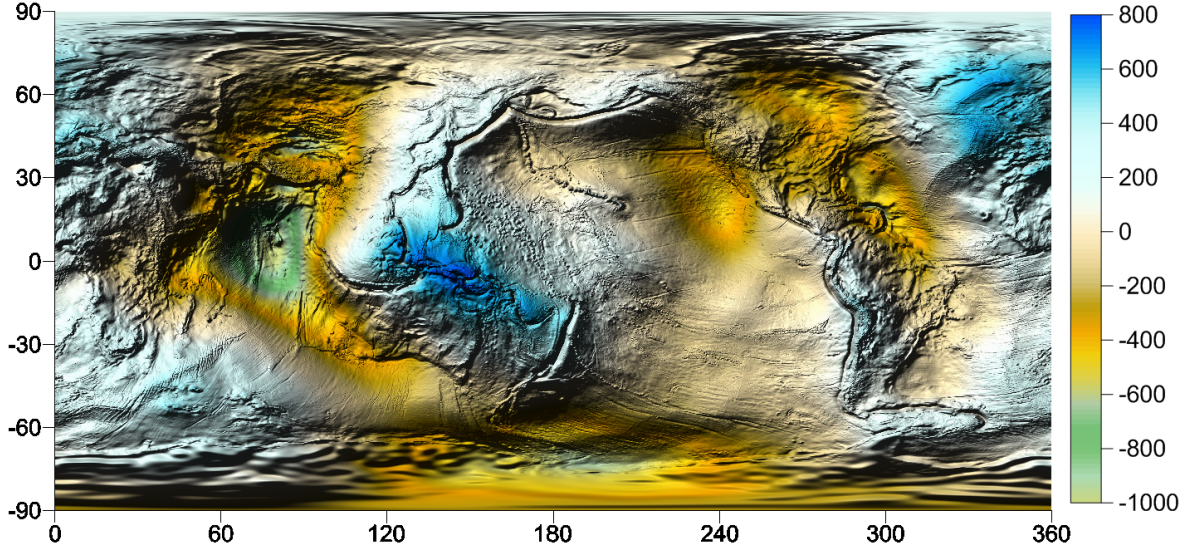


Figure 2.2.2: Earth: The disturbing potential solution  $T[m^2.s^{-2}]$  computed by FVM.

**Experiment 2.2.4.** In case of a global gravity field modelling we present the high-resolution gravity field modelling using the real geodetic data. The domain  $\Omega$  has been bounded by the WGS84 where the gravity disturbances from the DTU10-GRAV dataset have been prescribed and the upper boundary is at the altitude  $240\text{ km}$  above the reference ellipsoid where the disturbing potential generated from the GOCO03S has been given. The computational grid has been constructed using the number of divisions in  $L, B, H$  directions given by  $4320 \times 2160 \times 600$  (resolution:  $5' \times 5' \times 400\text{ m}$ ). The obtained FVM solution has been compared to EGM2008 and statistics of this comparison is presented in Table 3.14. Our results are depicted in Figure 2.2.2 and residuals between the FVM and EGM2008 are depicted in Figure 3.4.1. We can see that the standard deviation of our result and EGM2008 model is in the range of  $2\text{ cm}$  and on the oceans it is only  $1\text{ cm}$ . It indicates high precision of our method, thus we think that our approach can be used efficiently e.g. for monitoring of ocean variation.

**Experiment 2.2.5.** In the local experiment, we have considered the space above the Slovak Republic as our computational domain  $\Omega$ . The computational domain has

Statistics for res = T(EGM08) - T(FVM) [ $m^2s^{-2}$ ]			
	TOTAL	SEA	LAND
Number of nodes	9331200	6075501	3255699
Mean value	-0.0380	-0.0031	-0.1284
Max value	3.2781	1.7230	3.2781
Min value	-3.7383	-1.4920	-3.7383
St. deviation	0.1832	0.1170	0.2811

Table 2.7: Earth: Statistics of residuals  $T[m^2s^{-2}]$  on the bottom boundary  $\Gamma$ . TOTAL means statistics for the whole computational domain, SEA means statistics only over the sea and LAND means statistics over the lands.

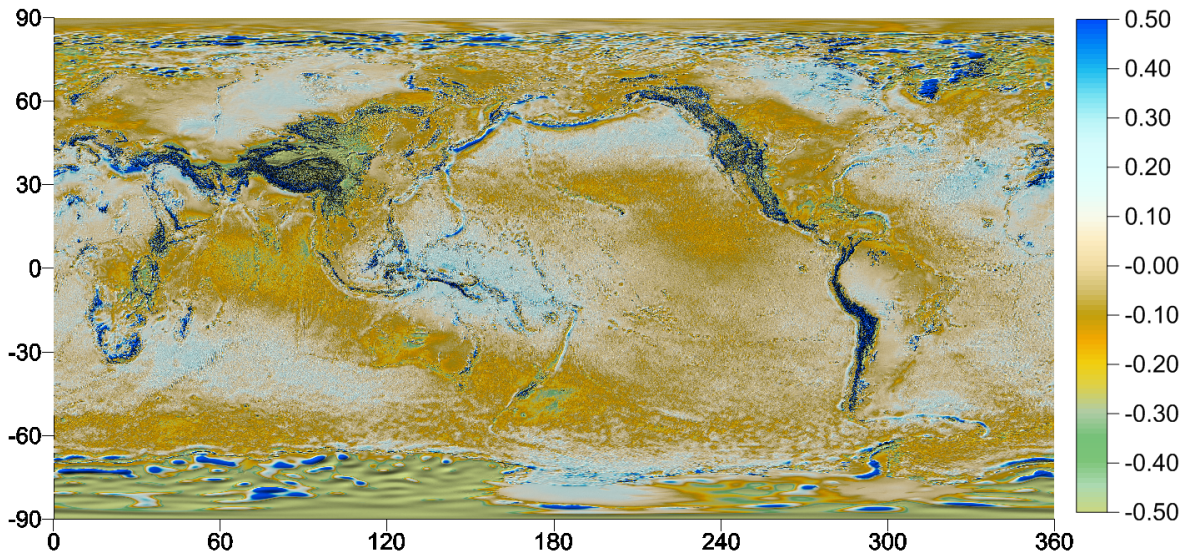


Figure 2.2.3: Earth: Residuals  $T[m^2.s^{-2}]$  between the disturbing potential computed by the FVM and EGM2008 solution on the bottom boundary  $\Gamma$ .

been defined by the ellipsoidal latitude and longitude in range  $B \in \langle 47.0^\circ, 55.5^\circ \rangle$  and  $L \in \langle 16.0^\circ, 23.0^\circ \rangle$ , respectively. The upper boundary is at 240 km above the WGS84 reference ellipsoid. The number of discretization intervals has been 840 in height, 630 in meridional and 300 in zonal directions. As input data on the bottom boundary  $\Gamma$  we used the surface gravity disturbances obtained from the original terrestrial gravimetric measurements that are available in the regular grid  $20'' \times 30''$  [17]. The disturbing potential on upper and side boundaries has been computed from the GOCO03S. Table 2.8 shows the GPS/levelling test of this model at 61 points. Standard deviation of residuals about 7 cm without additional fitting indicates better accuracy of our results in comparison with the present local quasigeoid model in Slovakia GMSQ-05C computed by different numerical techniques [39]. The mean value of residuals in our computation is different from EGM2008 or in GMSQ-05C which can indicate a shift of the national vertical datum. This shift value can be interesting for a unification of the local vertical datums with respect to the world height system, since the Dirichlet boundary data from GOCE are fully independent from leveling networks. The graphical representation of results is given in Figure 2.2.4.

	FVM Neumann BC	FEM	BEM	EGM2008	FFT gravsoft
Min. value	0.045	0.044	0.087	0.301	0.226
Mean value	0.232	0.248	0.183	0.437	0.385
Max. value	0.393	0.394	0.624	0.584	0.523
St. deviation	0.076	0.078	0.171	0.043	0.064

Table 2.8: SR: The GPS/leveling test [ $m$ ] at 61 points in area of Slovakia, where *FEM* denotes the solution presented in [13], *BEM* the solution published in [10] and *FFT* (*gravsoft*) denotes the solution presented in [39]. All solutions are obtained without applying the fitting method.

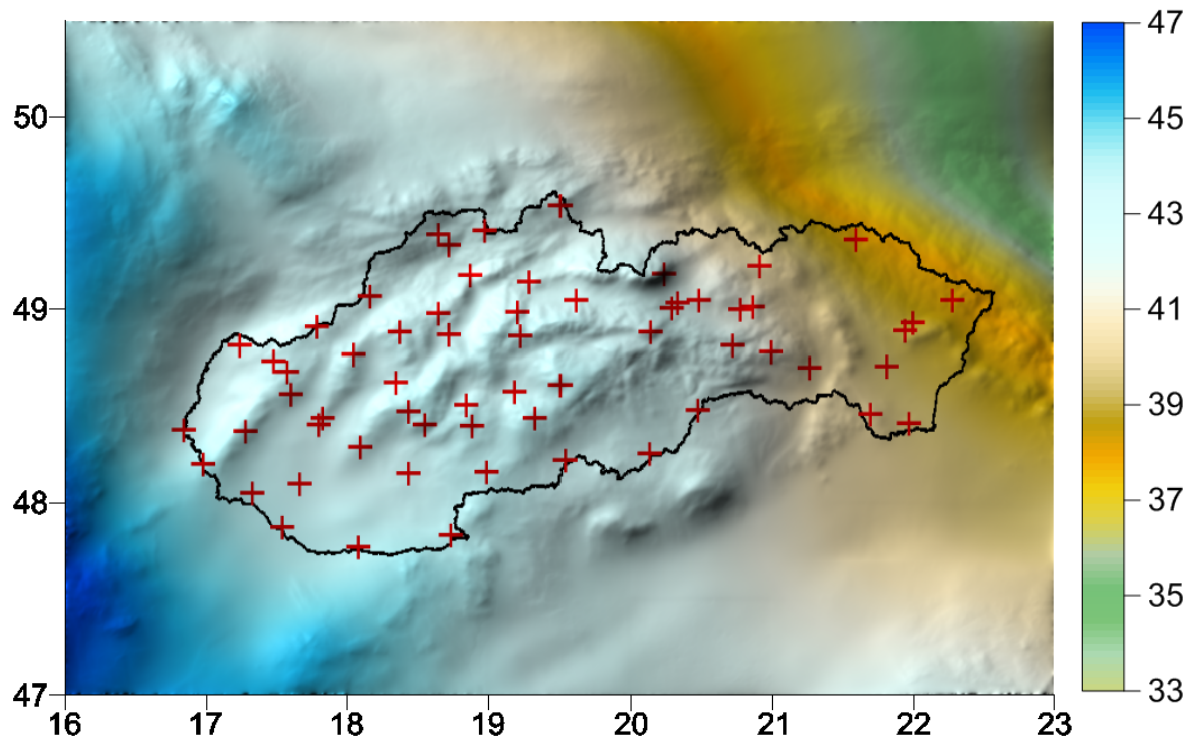


Figure 2.2.4: SR: Quasigeoid model  $\zeta[m]$  in the area of the Slovak Republic obtained by solving the Neumann FGBVP. Red crosses denote the distribution of 61 GPS/leveling points.

# Chapter 3

## Numerical solution of the oblique derivative boundary-value problem

In this section we are dealing with the oblique derivative FGBVP (1.3.23)-(1.3.25) and we present and discuss two novel approaches to solve it. It is worth to note that numerical solution of the oblique derivative BVPs by the FVM has many open questions and there are only few papers dealing with this topic [6, 7].

### 3.1 The central scheme for solving the oblique derivative BVP

The finite volume discretization of the equation (1.3.23) and the Dirichlet BC (1.3.25) follow the same principles as were explained in Chapter 2. In case of the oblique derivative BC on bottom boundary (1.3.24) we introduce a new treatment which will be discussed in 2D and 3D case.

The proposed approach has been published in [36] and [35].

Grid location	Compass notation
$i,j,k$	P
$i-1,j,k$	W
$i+1,j,k$	E
$i,j-1,k$	S
$i,j+1,k$	N
$i,j,k-1$	D
$i,j,k+1$	U
$i-\frac{1}{2},j,k$	w
$i+\frac{1}{2},j,k$	e
$i,j-\frac{1}{2},k$	s
$i,j+\frac{1}{2},k$	n
$i,j,k-\frac{1}{2}$	d
$i,j,k+\frac{1}{2}$	u

Table 3.1: Conversion between the mesh index and the compass notation.

### 3.1.1 2D case

We start by a splitting of the gradient in normal and tangential directions

$$\nabla T = \langle \nabla T, \vec{n} \rangle \vec{n} + \langle \nabla T, \vec{t} \rangle \vec{t} = \frac{\partial T}{\partial n} \vec{n} + \frac{\partial T}{\partial t} \vec{t}, \quad (3.1.1)$$

where  $\vec{n}$  is the normal vector and  $\vec{t}$  is the tangent vector to  $\Gamma$ .

Now we put (3.1.1) into (1.3.24) and obtain

$$\langle \nabla T, \vec{s} \rangle = \langle \frac{\partial T}{\partial n} \vec{n} + \frac{\partial T}{\partial t} \vec{t}, \vec{s} \rangle = \frac{\partial T}{\partial n} \langle \vec{n}, \vec{s} \rangle + \frac{\partial T}{\partial t} \langle \vec{t}, \vec{s} \rangle. \quad (3.1.2)$$

Thus the condition (1.3.24) is transformed into

$$\frac{\partial T}{\partial n} \langle \vec{n}, \vec{s} \rangle + \frac{\partial T}{\partial t} \langle \vec{t}, \vec{s} \rangle = \delta g. \quad (3.1.3)$$

For clearly arranged orientation in the FVM grid, we use a compass notation. The easy converting between compass notation and the cell indexing is given in Table 3.1. Then



$$\begin{aligned}\frac{\partial T}{\partial n} &= \frac{T_S - T_P}{|\mathbf{x}_S - \mathbf{x}_P|}, \\ \frac{\partial T}{\partial t} &= \frac{T_{ws} - T_{es}}{|\mathbf{x}_{ws} - \mathbf{x}_{es}|},\end{aligned}$$

where values  $T_{ws}, T_{we}$  are defined by

$$\begin{aligned}T_{ws} &= \frac{T_P + T_W + T_S + T_{WS}}{4}, \\ T_{es} &= \frac{T_P + T_E + T_S + T_{ES}}{4}.\end{aligned}$$

If we put these approximations into (3.1.3) we get a discrete form of the oblique derivative BC (1.3.24):

$$\langle \nabla T, \vec{s} \rangle = \frac{T_S - T_{Pj}}{|\mathbf{x}_S - \mathbf{x}_P|} \langle \vec{n}, \vec{s} \rangle + \frac{T_{ws} - T_{es}}{|\mathbf{x}_{ws} - \mathbf{x}_{es}|} \langle \vec{t}, \vec{s} \rangle = \delta g. \quad (3.1.7)$$

These equations are incorporated into the FVM linear system which is then solved.

### 3.1.2 3D case

We follow the similar way as was presented in 2D case, i.e. we start a by splitting the gradient in (1.3.24) into one normal and two tangential directions

$$\nabla T = \langle \nabla T, \vec{n} \rangle \vec{n} + \langle \nabla T, \vec{t}_1 \rangle \vec{t}_1 + \langle \nabla T, \vec{t}_2 \rangle \vec{t}_2 = \frac{\partial T}{\partial \vec{n}} \vec{n} + \frac{\partial T}{\partial \vec{t}_1} \vec{t}_1 + \frac{\partial T}{\partial \vec{t}_2} \vec{t}_2, \quad (3.1.8)$$

where  $\vec{n}$  is the normal vector and  $\vec{t}_1, \vec{t}_2$  are linearly independent tangent vectors to  $\Gamma \subset \partial\Omega \subset R^3$ . Then we put (3.1.8) into (1.3.24) to obtain

$$\langle \nabla T, \vec{s} \rangle = \left\langle \frac{\partial T}{\partial \vec{n}} \vec{n} + \frac{\partial T}{\partial \vec{t}_1} \vec{t}_1 + \frac{\partial T}{\partial \vec{t}_2} \vec{t}_2, \vec{s} \right\rangle = \frac{\partial T}{\partial \vec{n}} \langle \vec{n}, \vec{s} \rangle + \frac{\partial T}{\partial \vec{t}_1} \langle \vec{t}_1, \vec{s} \rangle + \frac{\partial T}{\partial \vec{t}_2} \langle \vec{t}_2, \vec{s} \rangle \quad (3.1.9)$$

and the BC (1.3.24) is transformed into the form

$$\frac{\partial T}{\partial \vec{n}} \langle \vec{n}, \vec{s} \rangle + \frac{\partial T}{\partial \vec{t}_1} \langle \vec{t}_1, \vec{s} \rangle + \frac{\partial T}{\partial \vec{t}_2} \langle \vec{t}_2, \vec{s} \rangle = \delta g. \quad (3.1.10)$$

We set approximations of normal and tangent vectors

$$\vec{n} = \left( \frac{x_D - x_P}{|\mathbf{x}_D - \mathbf{x}_P|}, \frac{y_D - y_P}{|\mathbf{x}_D - \mathbf{x}_P|}, \frac{z_D - z_P}{|\mathbf{x}_D - \mathbf{x}_P|} \right), \quad (3.1.11)$$

$$\vec{t}_1 = \left( \frac{x_{end} - x_{wsd}}{|\mathbf{x}_{end} - \mathbf{x}_{wsd}|}, \frac{y_{end} - y_{wsd}}{|\mathbf{x}_{end} - \mathbf{x}_{wsd}|}, \frac{z_{end} - z_{wsd}}{|\mathbf{x}_{end} - \mathbf{x}_{wsd}|} \right), \quad (3.1.12)$$

$$\vec{t}_2 = \left( \frac{x_{wnd} - x_{esd}}{|\mathbf{x}_{wnd} - \mathbf{x}_{esd}|}, \frac{y_{wnd} - y_{esd}}{|\mathbf{x}_{wnd} - \mathbf{x}_{esd}|}, \frac{z_{wnd} - z_{esd}}{|\mathbf{x}_{wnd} - \mathbf{x}_{esd}|} \right), \quad (3.1.13)$$

where  $\mathbf{x}_P = (x_P, y_P, z_P)$ ,  $\mathbf{x}_D$  are the coordinates of the added representative points and  $\mathbf{x}_{end}$ ,  $\mathbf{x}_{wsd}$ ,  $\mathbf{x}_{esd}$  and  $\mathbf{x}_{wnd}$  are the coordinates of the points on the bottom boundary  $\Gamma$ , see Fig. 3.1.2. In our testing numerical experiments, we consider the oblique vector in the form

$$\vec{s} = \left( \frac{x_C - x_d}{|\mathbf{x}_C - \mathbf{x}_d|}, \frac{y_C - y_d}{|\mathbf{x}_C - \mathbf{x}_d|}, \frac{z_C - z_d}{|\mathbf{x}_C - \mathbf{x}_d|} \right), \quad (3.1.14)$$

where  $\mathbf{x}_C$  is the point  $\mathbf{x}_C = (x_C, y_C, z_C) \in R^3$ . By  $T_P$  we denote the approximate value of the solution  $T$  in the finite volume  $P$  and we approximate the normal and tangential derivatives in (3.1.10) by

$$\frac{\partial T}{\partial \vec{n}} = \frac{T_D - T_P}{|\mathbf{x}_D - \mathbf{x}_P|}, \quad (3.1.15)$$

$$\frac{\partial T}{\partial \vec{t}_1} = \frac{T_{end} - T_{wsd}}{|\mathbf{x}_{end} - \mathbf{x}_{wsd}|}, \quad (3.1.16)$$

$$\frac{\partial T}{\partial \vec{t}_2} = \frac{T_{wnd} - T_{esd}}{|\mathbf{x}_{wnd} - \mathbf{x}_{esd}|}, \quad (3.1.17)$$

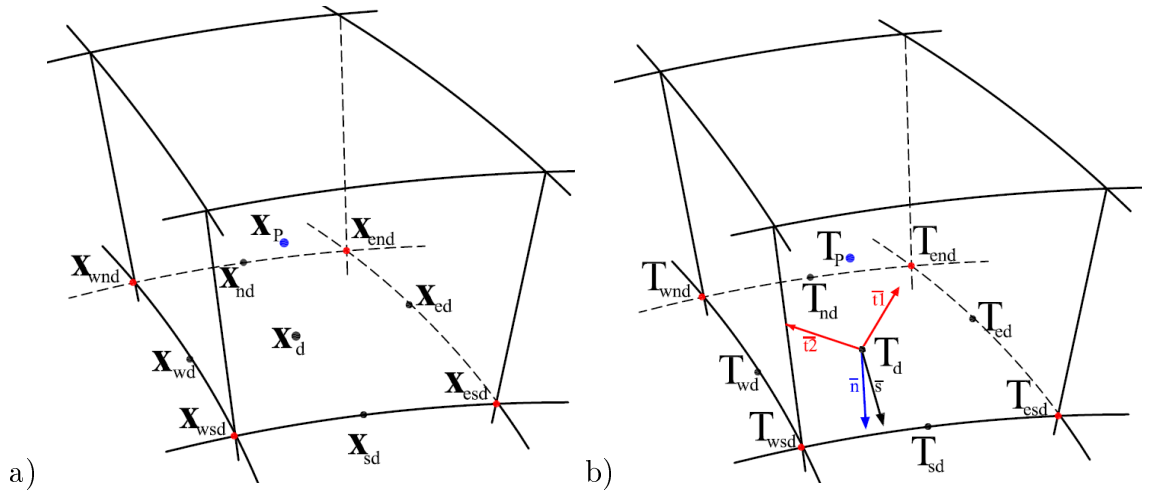


Figure 3.1.2: Illustration of the 3D computational grid for an approximation of the oblique derivative. a)  $\mathbf{x}_P$  denotes position vector of the center of volume  $p$ . b)  $T_P$  denotes the value of the disturbing potential in the center of finite volume  $p$ . Vectors  $\vec{t}_1$  and  $\vec{t}_2$  denote linearly independent tangent vectors to  $\Gamma$  and  $\vec{n}$  the normal vector to  $\Gamma$ .

where values  $T_{wnd}$ ,  $T_{end}$ ,  $T_{wsd}$ ,  $T_{esd}$  are defined by

$$\begin{aligned}
 T_{wnd} &= \frac{T_P + T_N + T_W + T_{NW} + T_D + T_{DN} + T_{DW} + T_{DNW}}{8}, \\
 T_{end} &= \frac{T_P + T_N + T_E + T_{NE} + T_D + T_{DN} + T_{DE} + T_{DNE}}{8}, \\
 T_{wsd} &= \frac{T_P + T_S + T_W + T_{SW} + T_D + T_{DS} + T_{DW} + T_{DSW}}{8}, \\
 T_{esd} &= \frac{T_P + T_S + T_E + T_{SE} + T_D + T_{DS} + T_{DE} + T_{DSE}}{8}.
 \end{aligned}$$

If we put these approximations into (3.1.10) we get a discrete form of the 3D oblique derivative BC (1.3.24)

$$\langle \nabla T, \vec{s} \rangle \approx \frac{T_D - T_P}{|\mathbf{x}_D - \mathbf{x}_P|} \langle \vec{n}, \vec{s} \rangle + \frac{T_{end} - T_{wsd}}{|\mathbf{x}_{end} - \mathbf{x}_{wsd}|} \langle \vec{t}_1, \vec{s} \rangle + \frac{T_{wnd} - T_{esd}}{|\mathbf{x}_{wnd} - \mathbf{x}_{esd}|} \langle \vec{t}_2, \vec{s} \rangle = \delta g. \quad (3.1.18)$$

These equations are incorporated into the FVM linear system which is then solved by a direct solver in the system Mathematica or by the Bi-CGSTAB solver in our C language program.

## 3.2 Numerical experiments using the central scheme

In this section, we present several numerical experiments which were done to test the proposed central numerical scheme. The numerical results have been compared with the exact solution. In Tables 3.2-3.5 the  $L_2(\Omega)$ -norm of differences between the exact and numerical solutions and EOC of the methods are presented. In experiments with real data we compare solution to the oblique derivative FGBVP using central scheme with solution of the Neumann-FGBVP.

### 3.2.1 2D Case

**Experiment 3.2.1.** In the numerical experiments of 2D case, the annulus between two circles with radii  $R_d = 1 m$  and  $R_u = 2 m$  has been used as a computational domain. As the Dirichlet BC (1.3.25) on the upper boundary, the chosen exact solution of (1.3.23) in the form  $T^* = -\log r$ , where  $r$  is the distance from the point mass source  $\mathbf{x}_C = (0.5, 0.35)$ , i.e.  $r = |\mathbf{x} - \mathbf{x}_C|$ , has been applied. As the oblique derivative BC on the bottom boundary, derivative of this exact solution, which is equal to  $1/r$ , has been considered. The plot of the solution to the BVP with the Neumann BC is depicted in Figure 3.2.1 a). The results of the BVP with the oblique derivative BC can be found in Table 3.2 and in Figure 3.2.1 b). One can observe that the proposed approach is second order accurate.

**Experiment 3.2.2.** For the second numerical experiment we have the same computational domain and BC on the upper boundary as in the previous experiment. The azimuth given by the original vector  $\vec{s}_1$ , the unit gradient vector of the exact solution computed by (3.1.6), has been modified by user chosen rotation angle  $\alpha$  to create a new vector  $\vec{s}$ , see Fig. 3.2.2. For this experiment we have chosen  $\alpha = 20^\circ$ . The coordinates of the point mass source have been  $\mathbf{x}_C = (-0.5, 0.6)$ . The  $L_2(\Omega)$ -norm of differences

	Central scheme	
$n_1 \times n_2$	$\ T^* - T\ _{L_2(\Omega)}$	EOC
$8 \times 2$	0.028261	-
$16 \times 4$	0.005400	2.38
$32 \times 8$	0.001113	2.27
$64 \times 16$	0.000263	2.08
$128 \times 32$	0.000064	2.01
$256 \times 64$	0.000014	2.02

Table 3.2: The  $L_2(\Omega)$ -norm and the EOC for the *Exp.* 3.2.1 with the oblique derivative BC computed with the shifted point mass source  $\mathbf{x}_C = (0.5, 0.35)$ .

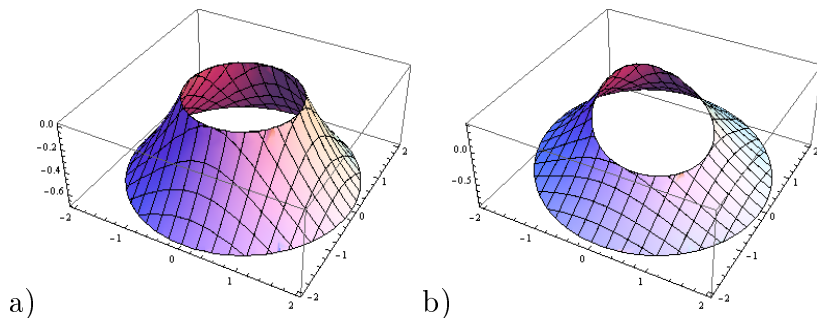


Figure 3.2.1: Graphs of the 2D solution to BVP with a) the Neumann BC b) the oblique derivative BC.

between the exact and numerical solutions and the EOC of the method are shown in Table 3.3.

We can see that also in case when the oblique vector does not have the same direction as the gradient of the solution, the proposed approach is second order accurate.

### 3.2.2 3D Case

**Experiment 3.2.3.** In 3D numerical experiments, as a computational domain a tesseroid bounded by two concentric spheres with radii  $R_d = 1 m$  and  $R_u = 2 m$ , and a coaxial cone with dimension  $(0, \pi/4) \times (0, \pi/4)$  has been used. As the Dirichlet BC (1.3.25), the exact solution of (1.3.23) in the form  $T^* = 1/r$  on the upper and the side boundaries, has been prescribed. As the oblique derivative BC on the bottom boundary, derivative

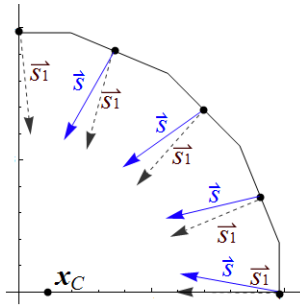


Figure 3.2.2: Illustration of creating  $\vec{s}$  by rotating of  $\vec{s}_1$  in 2D on the bottom boundary  $\Gamma$ .

	Central scheme	
$n_1 \times n_2$	$\ T^* - T\ _{L_2(\Omega)}$	EOC
$8 \times 2$	0.412322	-
$16 \times 4$	0.030709	3.74
$32 \times 8$	0.005261	2.54
$64 \times 16$	0.001076	2.28
$128 \times 32$	0.000244	2.14
$256 \times 64$	0.000057	2.09

Table 3.3: The  $L_2(\Omega)$ -norm and the EOC for the *Exp.* 3.2.2 with the oblique derivative BC when the oblique vector  $\vec{s}$  does not have direction of the solution gradient.

of this exact solution which is equal to  $-1/r^2$  has been applied. The point mass source has been  $\mathbf{x}_C = (-0.2, 0.1, 0.25)$ . The result can be seen in Table 3.4.

**Experiment 3.2.4.** For the second theoretical experiment, we have the same BCs on the upper and the side boundaries as in the previous one. The azimuth given by the original vector  $\vec{s}_1$ , the unit gradient vector of the exact solution computed by (3.1.14), has been modified by user chosen angle  $\alpha$  to create a new vector  $\vec{s}$ . For this experiment we have chosen  $\alpha = 20^\circ$ . The coordinates of the point mass source have been  $\mathbf{x}_C = (0.3, -0.2, 0.1)$ . The  $L_2(\Omega)$ -norm of differences between the exact and numerical solutions and the EOC of the method are shown in Table 3.5. We see that the method is second order accurate also in this case.

	Central scheme	
$n_1 \times n_2 \times n_3$	$\ T^* - T\ _{L_2(\Omega)}$	EOC
4×4×2	0.028622	-
8×8×4	0.006882	2.05
16×16×8	0.001450	2.24
32×32×16	0.000336	2.10
64×64×32	0.000081	2.05
128×128×64	0.000019	2.02

Table 3.4: The  $L_2(\Omega)$ -norm and the EOC for the *Exp.* 3.2.3 with oblique derivative BC computed from shifted point mass source  $\mathbf{x}_C = (-0.2, 0.1, 0.05)$ .

	Central scheme	
$n_1 \times n_2 \times n_3$	$\ T^* - T\ _{L_2(\Omega)}$	EOC
4×4×2	0.142463	-
8×8×4	0.022761	2.64
16×16×8	0.002728	3.06
32×32×16	0.000586	2.21
64×64×32	0.000137	2.08
128×128×64	0.000033	2.04

Table 3.5: The  $L_2(\Omega)$ -norm and the EOC for the *Exp.* 3.2.4 with the oblique derivative BC when the oblique vector  $\vec{s}$  does not have direction of the solution gradient.

### 3.2.3 3D numerical experiments with real data

**Experiment 3.2.5.** In case of global gravity field modelling we present the high-resolution gravity field modelling using real geodetic data. Computational domain and input data were the same as in *Experiment 2.2.4*. To calculate the oblique derivative vector, the ellipsoidal heights above the WGS84 have been generated from SRTM30 [5]. In Table 3.6 we can see the statistical characteristics of residuals between the solution of the FGBVP with the Neumann BC and FGBVP with the oblique derivative BC and disturbing potential generated from EGM2008.

We can see the improvement in the mean value of residual and standard deviation in lands areas when taking the oblique derivative BC into account, see Table 3.6, Fig. 3.2.3.

Statistics for res = T(EGM08) - T(FVM_e) [ $m^2s^{-2}$ ]						
	Neumann BC			oblique derivative BC		
	TOTAL	SEA	LAND	TOTAL	SEA	LAND
Mean value	-0.0380	-0.0031	-0.1284	-0.0364	-0.0031	-0.1136
Max. value	3.2781	1.7230	3.2781	2.0680	1.7230	2.0680
Min. value	-3.7383	-1.4920	-3.7383	-2.5620	-1.4920	-2.5620
St. deviation	0.1832	0.1170	0.2811	0.1699	0.1170	0.2515

Table 3.6: Earth: Statistics of residuals  $T[m^2s^{-2}]$  on the bottom boundary  $\Gamma$  between solutions to the GBVP with the oblique derivative BC and the Neumann BC.

**Experiment 3.2.6.** The local numerical experiment has dealt with the oblique derivative FGBVP above Slovakia similarly as *Experiment 2.2.5*. Input data was the same as in *Experiment 2.2.5*. Again, to calculate the oblique vector, the ellipsoidal heights above the WGS84 have been generated from SRTM30. The residuals between solutions to the FGBVP with the Neumann BC and the FGBVP with the oblique derivative BC can be seen in Fig. 3.2.4. The result of the GPS/leveling test at 61 points is presented in Table 3.7. The standard deviation of residuals at these GPS/levelling points in the

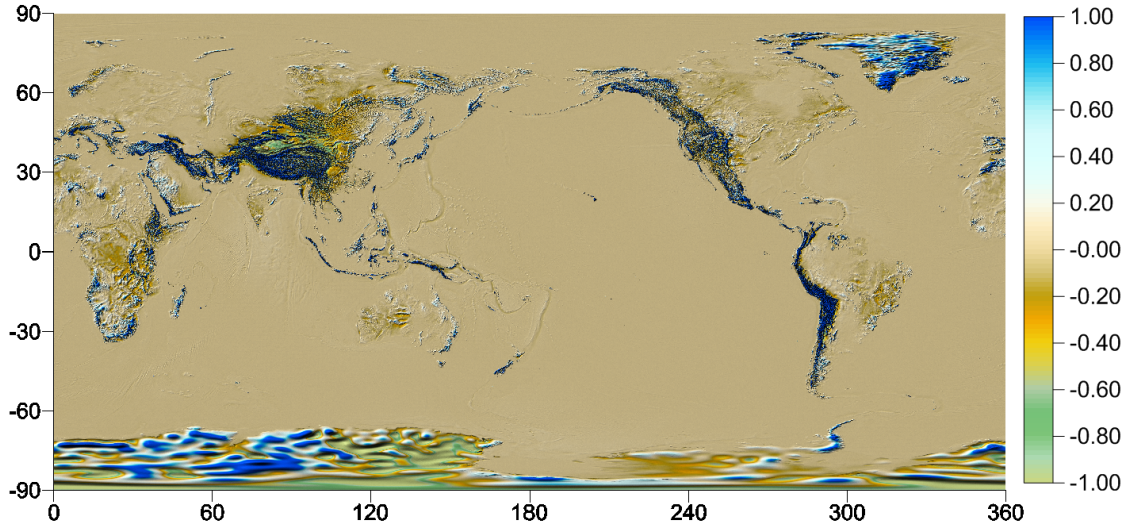


Figure 3.2.3: Earth: Differences  $T[m^2.s^{-2}]$  between solutions to the GBVP with the oblique derivative BC and the Neumann BC.

	FVM		EGM2008
	Neumann BC	oblique derivative BC	
Min. value	0.045	0.123	0.301
Mean value	0.232	0.274	0.437
Max. value	0.393	0.419	0.584
St. deviation	0.076	0.059	0.043

Table 3.7: SR: The GPS/leveling test [m] at 61 points in area of Slovakia.

case of the FGBVP with the Neumann BC is  $7.6\text{ cm}$ , while in the case of the BVP with the oblique derivative BC is only  $5.9\text{ cm}$ . Moreover, such a standard deviation is lower than the standard deviation of solutions obtained by the approaches based on the BEM or the FEM (see Table 2.8 in the previous Chapter).

### 3.2.4 A possible problems arising in the central scheme

In these numerical experiments we illustrate a possible problematic behaviour of the central scheme.

**Experiment 3.2.7.** For 2D numerical experiment we have the same computational

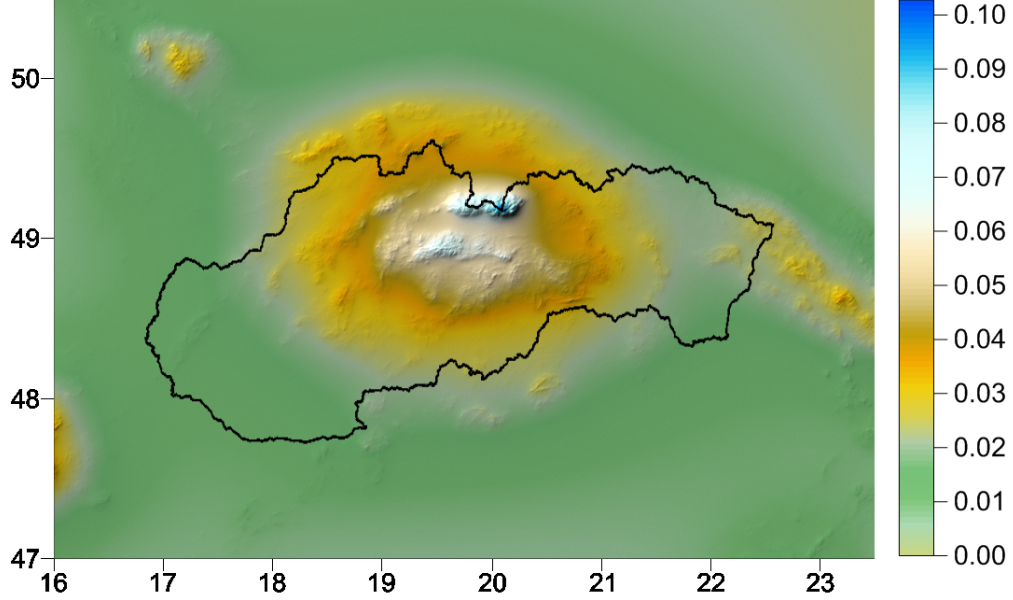


Figure 3.2.4: SR: The differences in quasigeoidal heights  $\zeta [m]$  obtained as a solution to the FGBVP with the oblique derivative BC and solution to the FGBVP with the Neumann BC.

domain and BC on the upper boundary as in *Experiment 3.2.1*. The azimuth given by the original vector  $\vec{s}_1$  has been modified by angle  $\alpha$  to create a new vector  $\vec{s}$ , for more details see *Experiment 3.2.1*. Moreover, to simulate the hill-valley-hill behaviour, we have multiplied this angle  $\alpha$  by  $\pm 1$ , i.e. when the value  $\alpha$  has been added to azimuth given by one vector, value  $-\alpha$  has been added to adjacent azimuths, see Fig. 3.2.5. For this experiment we have chosen  $\alpha = 20^\circ$ . The coordinates of the point mass source have been  $\mathbf{x}_C = (0.5, 0.6)$ . The  $L_2(\Omega)$ -norm of differences between the exact and numerical solutions and EOC of the method are shown in Table 3.8. One can observe high fluctuations in EOC in case of  $L_2(\Omega)$  as well as  $MAX(\Gamma)$ -norm which are caused by crossing of adjacent vectors, see Fig. 3.2.5.

**Experiment 3.2.8.** For 3D numerical experiment we have the same computational domain and BCs on the upper and the side boundaries as *Experiment 3.2.3* and similarly to 2D case, the azimuth given by the original vector  $\vec{s}_1$  has been again modified by angle  $\pm\alpha = 20^\circ$  to create a new vector  $\vec{s}$ . The point mass source has been

$n_1 \times n_2$	Central scheme			
	$\ T^* - T\ _{L_2(\Omega)}$	EOC	$\ T^* - T\ _{MAX(\Gamma)}$	EOC
$8 \times 2$	0.137785	-	0.629013	-
$16 \times 4$	0.273223	-0.98	0.447520	0.49
$32 \times 8$	0.073970	1.88	0.073060	2.61
$64 \times 16$	0.002050	5.17	0.014215	2.38
$128 \times 32$	0.001169	0.80	0.006873	1.04
$256 \times 64$	0.000402	1.53	0.002212	1.62

Table 3.8: The  $L_2(\Omega)$ -norm, the  $MAX(\Gamma)$ -norm and the EOC for the *Exp.* 3.2.7 with the oblique derivative BC when the oblique vector  $\vec{s}$  does not have direction of the solution gradient.

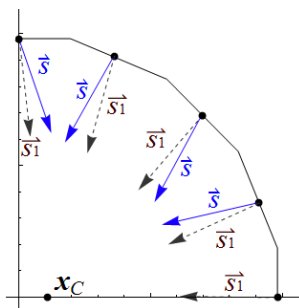


Figure 3.2.5: Illustration of creating  $\vec{s}$  by rotating of  $\vec{s}_1$  by an angle  $\pm\alpha$  in 2D case.

$\mathbf{x}_C = (0.1, -0.2, 0.1)$ . The  $L_2(\Omega)$ -norm of differences between the exact and numerical solutions and EOC of the method are shown in Table 3.9. One can observe the same behaviour as was obtained in 2D case, i.e., the EOC varies for both norms. This drawback is again caused by the crossing of the adjacent oblique vectors.

### 3.3 The up-wind scheme for solving oblique derivative BVP

In this section we discuss a new point of view of the oblique derivative BC (1.3.24) and we treat it as an advection equation.

$n_1 \times n_2 \times n_3$	Central scheme			
	$\ T^* - T\ _{L_2(\Omega)}$	EOC	$\ T^* - T\ _{MAX(\Gamma)}$	EOC
$8 \times 8 \times 4$	0.061529	-	0.351144	-
$16 \times 16 \times 8$	0.146351	-1.25	0.209212	0.75
$32 \times 32 \times 16$	0.058753	1.31	0.050549	2.05
$64 \times 64 \times 32$	0.008090	2.86	0.053722	2.64
$128 \times 128 \times 64$	0.004520	0.83	0.024245	0.84

Table 3.9: The  $L_2(\Omega)$ -norm, the  $MAX(\Gamma)$ -norm and the EOC for the *Exp.* 3.2.8 with oblique derivative BC when the oblique vector  $\vec{s}$  does not have direction of the solution gradient.

Let us rewrite (1.3.24) in the formally equivalent form

$$\langle \nabla T, \vec{s} \rangle - \langle T \nabla, \vec{s} \rangle = \delta g. \quad (3.3.1)$$

We add one row of volumes under the bottom boundary, see Fig. 3.3.1, and integrate (3.3.1) over one of the added finite volume  $p$

$$\int_p \langle \nabla T, \vec{s} \rangle dx - \int_p \langle T \nabla, \vec{s} \rangle dx = \int_p \delta g dx. \quad (3.3.2)$$

Using a constant representation of the solution  $T$  on the finite volume  $p$  denoted by  $\bar{T}_p$  and applying the divergence theorem to the left-hand side of the equation (3.3.2) we obtain

$$\sum_{q \in N(p)} \int_{\partial p} T \langle \vec{s}, \vec{n}_{pq} \rangle ds - \sum_{q \in N(p)} \bar{T}_p \int_{\partial p} \langle \vec{s}, \vec{n}_{pq} \rangle ds = \int_p \delta g dx. \quad (3.3.3)$$

Denoting a constant representative value of the solution on the interface  $e_{pq}$  by  $\bar{T}_{pq}$  and a measure of the finite volume  $p$  by  $m(p)$  yields

$$\sum_{q \in N(p)} \bar{T}_{pq} \int_{\partial p} \langle \vec{s}, \vec{n}_{pq} \rangle ds - \sum_{q \in N(p)} \bar{T}_p \int_{\partial p} \langle \vec{s}, \vec{n}_{pq} \rangle ds = \delta g m(p). \quad (3.3.4)$$

When we denote

$$\bar{s}_{pq} = \int_{\partial p} \langle \vec{s}, \vec{n}_{pq} \rangle ds, \quad (3.3.5)$$

we finally obtain the balance law in the form

$$\sum_{q \in N(p)} \bar{s}_{pq} (\bar{T}_{pq} - \bar{T}_p) = \delta g m(p). \quad (3.3.6)$$

In our approach the upwind principle is used where we define

$$\bar{T}_{pq} = \bar{T}_p, \quad \text{if } \bar{s}_{pq} > 0, \quad (3.3.7)$$

$$\bar{T}_{pq} = \bar{T}_q, \quad \text{if } \bar{s}_{pq} < 0, \quad (3.3.8)$$

which correspond to the inflow part to the finite volume  $p$  ( $\bar{s}_{pq} < 0$ ) and outflow part to the finite volume  $p$  ( $\bar{s}_{pq} > 0$ ). The most natural choice for reconstructions  $\bar{T}_p$  and  $\bar{T}_q$  is given by

$$\bar{T}_p = T_p, \quad (3.3.9)$$

$$\bar{T}_q = T_q. \quad (3.3.10)$$

Then the final form of an approximation to the oblique derivative BC (1.3.24) can be written as

$$\sum_{q \in N(p)^{in}} \bar{s}_{pq} (T_q - T_p) = \delta g m(p), \quad (3.3.11)$$

where  $N(p)^{in}$  is a set of neighbours at the inflow boundaries of the finite volume  $p$ .

### 3.4 Numerical experiments using the up-wind scheme

In this section, we present several numerical experiments which were performed in order to test the proposed up-wind scheme.

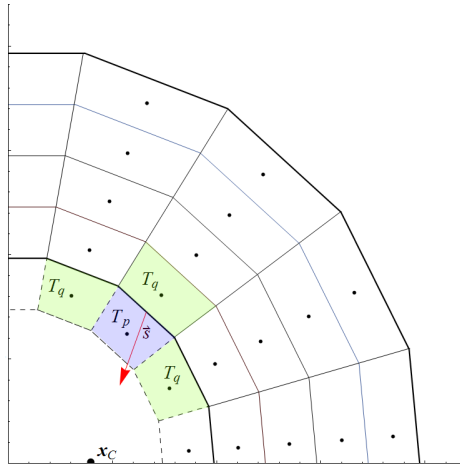


Figure 3.3.1: Illustration of the 2D FVM grid. The dashed lines denote the boundaries of added finite volumes, by blue colour is depicted the volume of interest and by green its neighbours. The vectors  $\vec{s}$  are depicted by red.

$n_1 \times n_2$	Up-wind scheme				Central scheme			
	$\ T^* - T\ _{L_2(\Omega)}$	EOC	$\ T^* - T\ _{MAX(\Gamma)}$	EOC	$\ T^* - T\ _{L_2(\Omega)}$	EOC	$\ T^* - T\ _{MAX(\Gamma)}$	EOC
$8 \times 2$	0.043461	-	0.137448	-	0.028261	-	0.071431	-
$16 \times 4$	0.012002	1.85	0.038109	1.95	0.005400	2.38	0.009351	2.93
$32 \times 8$	0.004297	1.48	0.014736	1.37	0.001113	2.27	0.002370	1.98
$64 \times 16$	0.001794	1.26	0.006325	1.26	0.000263	2.08	0.000748	1.66
$128 \times 32$	0.000816	1.10	0.002929	1.11	0.000064	2.01	0.000260	1.52
$256 \times 64$	0.000389	1.06	0.001409	1.05	0.000014	2.02	0.000102	1.34

Table 3.10: The  $L_2(\Omega)$ -norm,  $MAX(\Gamma)$ -norm and the EOC for the *Exp.* 3.4.1 and *Exp.* 3.2.1 with the oblique derivative BC computed from shifted point mass source  $\mathbf{x}_C = (0.5, 0.35)$ .

### 3.4.1 2D Case

**Experiment 3.4.1.** In the first experiment, we have considered the oblique derivative BC (1.3.24) on the bottom boundary, the BCs on the upper boundary as in *Experiment* 3.2.1. The point mass source has been shifted to the point  $\mathbf{x}_C = (0.5, 0.35)$ . The comparison of central scheme and up-wind scheme can be found in Table 3.10. One can observe that the  $L_2(\Omega)$  and  $MAX(\Gamma)$  norms in case of up-wind scheme are approximately of first order. We can also observe the error in  $MAX(\Gamma)$ -norm of the central scheme decreases its values also to 1.

$n_1 \times n_2$	Up-wind scheme				Central scheme			
	$\ T^* - T\ _{L_2(\Omega)}$	EOC	$\ T^* - T\ _{MAX(\Gamma)}$	EOC	$\ T^* - T\ _{L_2(\Omega)}$	EOC	$\ T^* - T\ _{MAX(\Gamma)}$	EOC
$8 \times 2$	0.297626	-	0.745665	-	0.137785	-	0.6290	-
$16 \times 4$	0.131778	1.17	0.298533	1.32	0.273223	-0.98	0.447520	0.49
$32 \times 8$	0.045405	1.53	0.120554	1.31	0.073970	1.88	0.073060	2.61
$64 \times 16$	0.017239	1.39	0.0534402	1.17	0.002050	5.17	0.014215	2.38
$128 \times 32$	0.007523	1.19	0.021405	1.33	0.001169	0.80	0.006873	1.04
$256 \times 64$	0.003536	1.08	0.009175	1.21	0.000402	1.53	0.002212	1.62

Table 3.11: The  $L_2(\Omega)$ -norm,  $MAX(\Gamma)$ -norm and the EOC for the *Exp.* 3.4.2 and *Exp.* 3.2.7 when the oblique vector  $\vec{s}$  does not have direction of the solution gradient.

**Experiment 3.4.2.** For the second 2D numerical experiment we have chosen a comparison between the up-wind and central scheme presented in *Experiment* 3.2.7. As we can see in Table 3.11 the EOC,  $L_2(\Omega)$ -norm and  $MAX(\Gamma)$ -norm for the up-wind method remains stable while the central scheme does not.

### 3.4.2 3D Case

**Experiment 3.4.3.** In 3D experiments, we have also compared the central and up-wind scheme. We have the same computation domain, BCs on the upper and the side boundaries as in *Experiment* 3.2.3. The point mass source has been shifted to point  $\mathbf{x}_C = (-0.2, 0.1, 0.25)$ . The comparison of solutions obtained by implementing the central and up-wind scheme is presented in Table 3.12.

We can see the same behaviour as was observed in 2D experiments, i.e. both methods are stable. Although the EOC for  $L_2$ -norm in case of up-wind scheme is less than the EOC for central one. On the other hand in case of the EOC for  $MAX(\Gamma)$ -norm, the value for central scheme is less than 2.

**Experiment 3.4.4.** For the last 3D numerical experiment we choose comparison between two our method on *Experiment* 3.2.8. Results are shown in Table 3.13.

$n_1 \times n_2 \times n_3$	Up-wind scheme				Central scheme			
	$\ T^* - T\ _{L_2(\Omega)}$	EOC	$\ T^* - T\ _{MAX(\Gamma)}$	EOC	$\ T^* - T\ _{L_2(\Omega)}$	EOC	$\ T^* - T\ _{MAX(\Gamma)}$	EOC
$4 \times 4 \times 2$	0.106407	-	0.113491	-	0.028622	-	0.044464	-
$8 \times 8 \times 4$	0.036369	1.54	0.0484544	1.22	0.006882	2.05	0.008890	2.32
$16 \times 16 \times 8$	0.014450	1.33	0.024185	1.01	0.001450	2.24	0.003150	1.49
$32 \times 32 \times 16$	0.006244	1.21	0.012070	1.01	0.000336	2.10	0.001083	1.54
$64 \times 64 \times 32$	0.002895	1.10	0.006010	1.00	0.000081	2.05	0.000334	1.69
$128 \times 128 \times 64$	0.001392	1.05	0.002865	1.06	0.000019	2.02	0.000105	1.66

Table 3.12: The  $L_2(\Omega)$ -norm,  $MAX(\Gamma)$ -norm and the EOC for the *Exp.* 3.4.3 and *Exp.* 3.2.3 with the oblique derivative BC experiment with the shifted point mass source  $\mathbf{x}_C = (-0.2, 0.1, 0.25)$ .

One can observe that in both experiments in 3D, either central or up-wind scheme shows the same behaviour as was obtained in experiments in 2D.

$n_1 \times n_2 \times n_3$	Up-wind scheme				Central scheme			
	$\ T^* - T\ _{L_2(\Omega)}$	EOC	$\ T^* - T\ _{MAX(\Gamma)}$	EOC	$\ T^* - T\ _{L_2(\Omega)}$	EOC	$\ T^* - T\ _{MAX(\Gamma)}$	EOC
$8 \times 8 \times 4$	0.177728	-	0.362022	-	0.061529	-	0.3511	-
$16 \times 16 \times 8$	0.059441	1.58	0.177806	1.03	0.146351	-1.25	0.209212	0.75
$32 \times 32 \times 16$	0.022542	1.39	0.083563	1.08	0.058753	1.31	0.050549	2.05
$64 \times 64 \times 32$	0.010819	1.05	0.041756	1.00	0.008090	2.86	0.053722	2.64
$128 \times 128 \times 64$	0.005143	1.07	0.019506	1.13	0.004520	0.83	0.024245	0.84

Table 3.13: The  $L_2(\Omega)$ -norm,  $MAX(\Gamma)$ -norm and the EOC for the *Exp.* 3.4.4 and *Exp.* 3.2.8 with the 3D oblique derivative BC when the oblique vector  $\vec{s}$  does not have direction of the solution gradient.

### 3.4.3 3D numerical experiments with real data

**Experiment 3.4.5.** In case of global gravity field modelling we compare the solution obtained by the up-wind scheme with the solution achieved by the central scheme presented in *Experiment* 3.2.5 and solution obtained from solving the Neumann-FGBVP presented in *Experiment* 2.2.4. Results can be seen in Table 3.14 and difference between solutions of central and up-wind scheme was depicted in Figure 3.4.1.

One can observe the comparable statistics for central and up-wind approaches, i.e.

Statistics for $\text{res} = T(\text{EGM08}) - T(\text{FVM}) [m^2s^{-2}]$									
	Neumann BC			oblique derivative BC					
	TOTAL	SEA	LAND	TOTAL	SEA	LAND	TOTAL	SEA	LAND
				central scheme			up-wind scheme		
Min value	-3.7383	-1.4920	-3.7383	-2.5620	-1.4920	-2.5620	-3.3150	-1.4920	-3.3150
Mean value	-0.0380	-0.00319	-0.1284	-0.0364	-0.0031	-0.1136	-0.0372	-0.0031	-0.1165
Max value	3.2781	1.7230	3.2781	2.0680	1.7230	2.0680	2.6390	1.7230	2.6390
St. deviation	0.1832	0.1170	0.2811	0.1699	0.1170	0.2515	0.1801	0.1170	0.2655

Table 3.14: Earth: Statistics of residuals  $T[m^2s^{-2}]$  on the bottom boundary  $\Gamma$ .

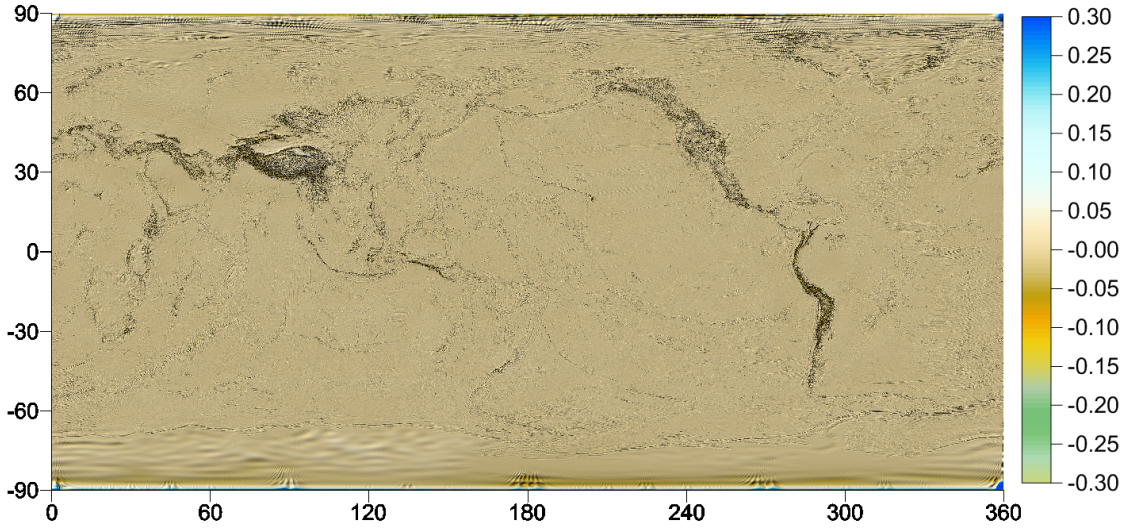


Figure 3.4.1: Earth: Residuals of the disturbing potential  $T[m^2.s^{-2}]$  between the FVM solution obtained by implementing the central scheme and the FVM solution obtained by implementing up-wind scheme.

the both schemes can be used in practise approach.

**Experiment 3.4.6.** In case of local gravity field modelling in area of Slovakia we again compare solution obtained by the up-wind scheme with the central scheme solution presented in *Experiment 3.4.6* and the solution obtained by solving of the Neumann-FGBVP presented in *Experiment 2.2.5*.

Results can be seen in Table 3.15 and difference between the central and the up-wind scheme is depicted in Figure 3.4.2. One can observe that solutions achieved by implementing the central and up-wind scheme are very similar to each other, they differ

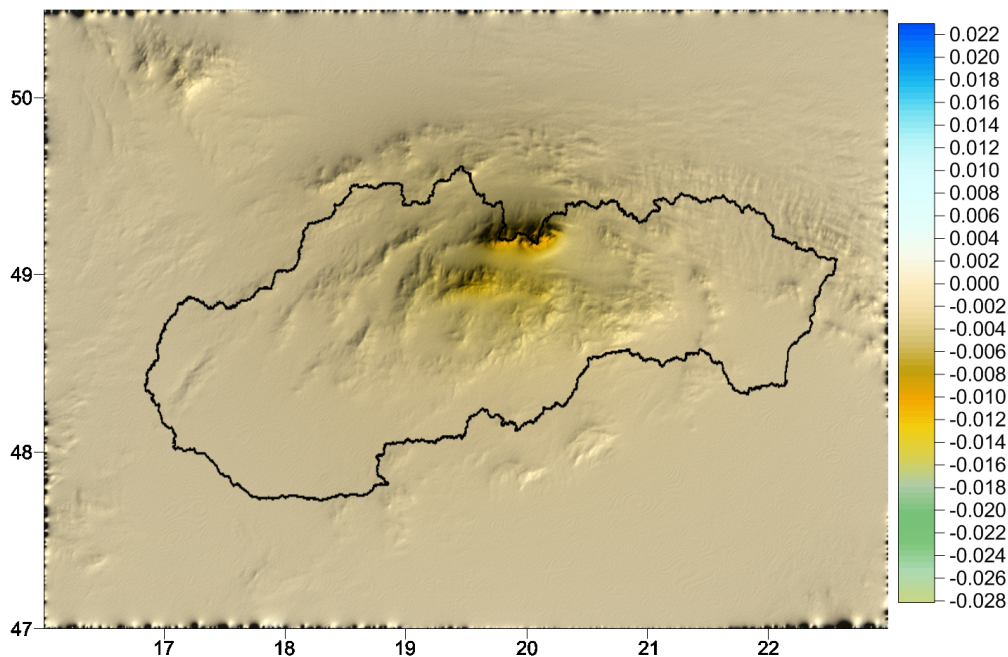


Figure 3.4.2: SR: Differences in the quasigeoidal heights  $\zeta[m]$  between the up-wind scheme and the central scheme.

only in several millimeters.

	FVM			EGM2008
	Neumann BC	oblique derivative BC		
		central scheme	up-wind scheme	
Min value	0.045	0.123	0.131	0.301
Mean value	0.232	0.274	0.279	0.437
Max value	0.393	0.419	0.421	0.584
St. deviation	0.076	0.059	0.058	0.043

Table 3.15: SR: The GPS/leveling test  $[m]$  at 61 points in area of Slovakia.

## Chapter 4

# On an iterative approach to solving the non-linear geodetic boundary-value problem

Finally we present the numerical solution of the NFGBVP defined in the bounded domain, i.e.

$$\Delta T = 0 \text{ in } \Omega, \quad (4.0.1)$$

$$|\nabla(T + U)| = g \text{ on } \Gamma, \quad (4.0.2)$$

$$T = T_{SAT} \text{ on } \partial\Omega - \Gamma. \quad (4.0.3)$$

The iterative procedure for solving the NFGBVP (4.0.1)-(4.0.3) is defined as follows, for detailed formulation see Chapter 1,

$$\Delta T^{n+1} = 0 \text{ in } \Omega, \quad (4.0.4)$$

$$\langle \nabla T^{n+1}, \vec{v}^n \rangle = g - \langle \nabla U, \vec{v}^n \rangle \text{ on } \Gamma, \quad (4.0.5)$$

$$T^{n+1} = T_{SAT} \text{ on } \partial\Omega - \Gamma, \quad (4.0.6)$$

where we solve in every iteration the oblique derivative GBVP for  $T^{n+1}$  with prescribed oblique derivative vector  $\vec{v}^n$  computed by (1.3.13).

Since we solve the problem iteratively, we need a stopping criterion. To that goal

we use a difference of two successive iterations and stop the procedure, if in each point the inequality

$$|T^n - T^{n+1}| < \varepsilon, \quad (4.0.7)$$

holds, where  $\varepsilon$  means a user-specified small real number.

This formulation of the NFGBVP and its iterative solution will be published in [34].

## 4.1 Numerical experiments

In these numerical experiments, we compare iterative solutions obtained by the up-wind and the central schemes.

### 4.1.1 2D Case

**Experiment 4.1.1.** Computational domain and BC on upper boundary is the same as in *Experiment 3.2.2*. The point mass source has been  $\mathbf{x}_C = (0.35, 0.25)$ . We start our iterations by solving the BVP with oblique BC (4.0.6) by the methods introduced in the previous Chapter. The initial oblique vector  $\vec{v}^0$  has been given by rotation of  $\vec{s}_1$  (see *Experiment 3.2.1*) by angle  $\alpha = 5^\circ$ , see Fig. 3.2.2. For this experiment we have chosen stopping criterium  $\varepsilon = 10^{-3}$  and the maximum iteration  $Iter_{Max} = 40$ . For a comparison between the central and the up-wind scheme see Table 4.1. One can observe oscillation of the central scheme in solution to the non-linear BVP, while the up-wind scheme behaves stable, see Fig. 4.1.1.

### 4.1.2 3D Case

**Experiment 4.1.2.** In the first 3D experiment, the computational domain and BCs on the upper and side boundaries are the same as in *Experiment 3.2.3*. The point mass source has been  $\mathbf{x}_s = (0.1, 0.2, 0.1)$  and the oblique vector  $\vec{v}^0$  has been given by rotation

$n_1 \times n_2$	Iterative solution Up-wind scheme					Iterative solution Central scheme				
	$\ T^* - T\ _{L_2(\Omega)}$	EOC	$\ T^* - T\ _{MAX(\Gamma)}$	EOC	Iter.	$\ T^* - T\ _{L_2(\Omega)}$	EOC	$\ T^* - T\ _{MAX(\Gamma)}$	EOC	Iter.
$8 \times 2$	0.071137	-	0.024393	-	8	0.008884	-	0.038362	-	6
$16 \times 4$	0.023921	1.57	0.0118496	1.14	6	0.001072	3.05	0.002779	3.78	5
$32 \times 8$	0.009133	1.38	0.0052429	1.06	5	0.000240	2.15	0.000583	2.25	4
$64 \times 16$	0.003915	1.22	0.002548	1.04	5	0.000063	1.92	0.000153	1.95	6
$128 \times 32$	0.001805	1.11	0.001224	1.15	5	0.000040	0.62	0.000038	2.02	9
$256 \times 64$	0.000866	1.05	0.000602	1.01	4	0.000138	-1.75	0.000142	-1.91	10
$512 \times 128$	0.000420	1.04	0.000296	1.02	5	0.002142	-3.95	0.001577	-3.46	20

Table 4.1: The  $L_2(\Omega)$ -norm,  $MAX(\Gamma)$ -norm and the EOC for the *Exp.* 4.1.1.

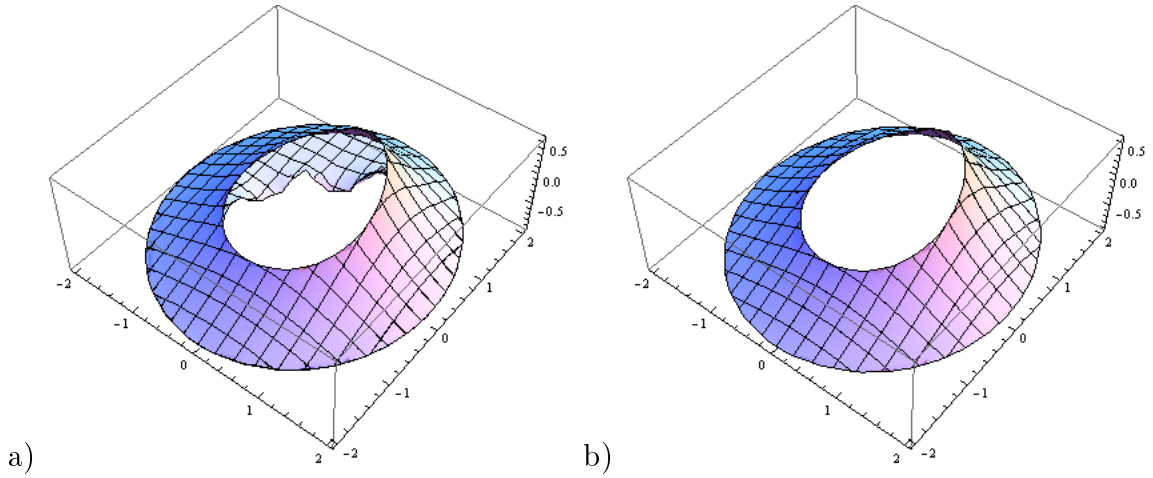


Figure 4.1.1: a) Illustration of possible oscillation in central scheme iterative solution. b) Illustration of the solution obtained by up-wind scheme, *Exp.* 3.2.2.

of  $\vec{s}_1$  by angle  $\alpha = 5^\circ$ . For this experiment we have chosen  $\varepsilon = 10^{-3}$  and the maximum iteration  $Iter_{Max} = 40$ . For a comparison between the central and the up-wind scheme, see Table 4.2. We can observe decrease of the EOC for the central scheme.

$n_1 \times n_2 \times n_3$	Iterative solution Up-wind scheme					Iterative solution Central scheme				
	$\ T^* - T\ _{L_2(\Omega)}$	EOC	$\ T^* - T\ _{MAX(\Gamma)}$	EOC	Iter.	$\ T^* - T\ _{L_2(\Omega)}$	EOC	$\ T^* - T\ _{MAX(\Gamma)}$	EOC	Iter
$8 \times 8 \times 4$	0.035859	-	0.027127	-	8	0.016172	-	0.016734	-	7
$16 \times 16 \times 8$	0.017597	1.17	0.012744	1.08	6	0.004119	1.97	0.002685	2.63	7
$32 \times 32 \times 16$	0.007895	1.15	0.005708	1.15	5	0.000963	2.09	0.000635	2.07	8
$64 \times 64 \times 32$	0.003657	1.11	0.002677	1.01	5	0.000229	2.07	0.000347	0.87	9
$128 \times 128 \times 64$	0.001753	1.06	0.001140	1.08	5	0.000056	2.02	0.000266	0.38	8
$256 \times 256 \times 128$	0.000842	1.05	0.000546	1.06	6	0.000014	2.03	0.000194	0.45	9

Table 4.2: The  $L_2(\Omega)$ -norm,  $MAX(\Gamma)$ -norm and the EOC for the *Exp.* 4.1.2.

### 4.1.3 3D numerical experiments with real data

**Experiment 4.1.3.** With respect to results obtained in the above numerical experiments, in experiments with the real data we use the up-wind scheme only. The global numerical experiment has dealt with the high-resolution global gravity field modeling in the computational domain  $\Omega$  bounded by the bottom boundary approximating the real Earth's surface created by using heights generated from SRTM30 PLUS and by a surface at height of 240 km above WGS84. The number of divisions was  $4320 \times 2160 \times 600$  leading to the resolution  $5' \times 5' \times 400 m$ . We start the iterations by solving the linearized FGBVP consisting of gravity disturbances interpolated from the DTU10-GRAV applied on the bottom boundary. The total gravity  $g$  has been calculated as a sum of the surface gravity disturbance and the normal gravity. On the upper boundary the disturbing potential generated from GOCO03s was prescribed. The stopping criterium was  $\epsilon = 10^{-3}[m^2s^{-2}]$  and 10 iterations were needed to earn it. The FVM solutions obtained in each iteration are compared with EGM2008. Statistical characteristics of residuals are presented in Table 4.3. Figure 4.1.2 depicts differences

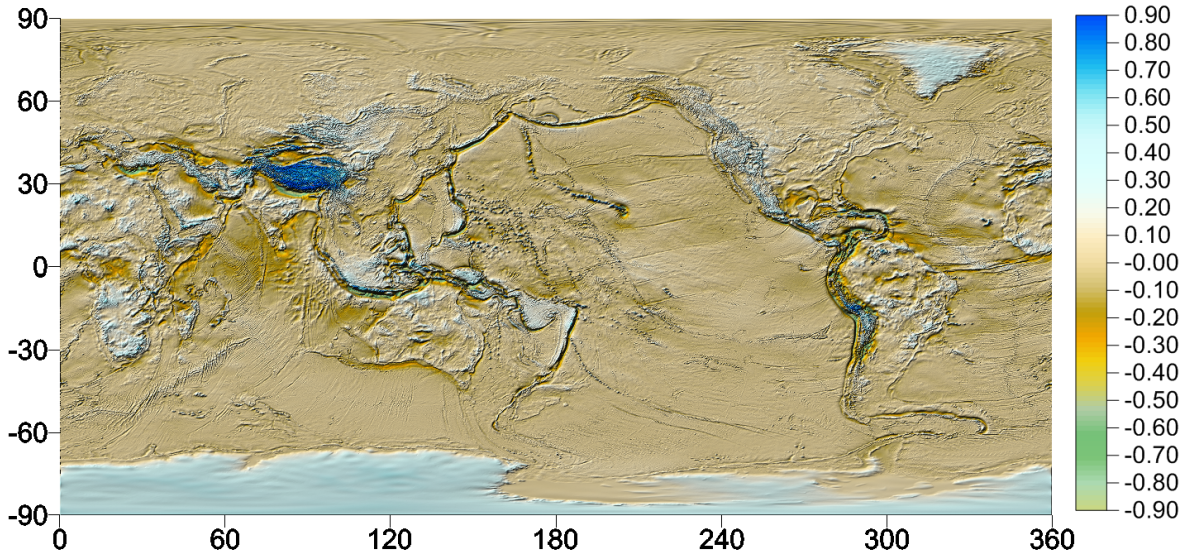


Figure 4.1.2: Earth: Differences in  $T[m^2s^{-2}]$  between  $10^{th}$  and  $1^{st}$  iteration, representing the numerically obtained linearization error.

Iter.	Min. value		Mean value		Max. value		St. dev.	
	$1^{st}$	$10^{th}$	$1^{st}$	$10^{th}$	$1^{st}$	$10^{th}$	$1^{st}$	$10^{th}$
TOTAL	-3.3150	-2.0760	-0.0372	-0.0347	2.6390	1.3330	0.1801	0.1581
SEA	-1.4920	-1.0280	-0.0031	-0.0031	2.0820	1.2270	0.1170	0.1081
LAND	-3.3150	-2.0760	-0.1165	-0.1082	2.6390	1.3330	0.2655	0.2358

Table 4.3: Earth: Statistics of residuals  $[m^2s^{-2}]$  between the disturbing potential obtained by solving the NFGBVP and the disturbing potential generated from EGM2008 in the global experiment.

between the  $10^{th}$  and  $1^{st}$  iteration. They represent the numerically obtained linearization error in the linearized FGBVP. One can observe that our iterative approach improves solution mainly in areas of high mountains (e.g. in Himalaya region they reach  $20\text{ cm}$ ) as well as in areas along the ocean trenches (varying from  $-2.5\text{ cm}$  to  $2.5\text{ cm}$ ).

**Experiment 4.1.4.** The local numerical experiment was performed in the domain above Slovakia bounded by  $\varphi \in \langle 47.0^\circ, 50.5^\circ \rangle$  and  $\lambda \in \langle 16.0^\circ, 23.0^\circ \rangle$ . The bottom boundary was created using SRTM30 PLUS and the upper boundary was at the height of 240 km above the WGS84. The resolution with respect to latitude and longitude

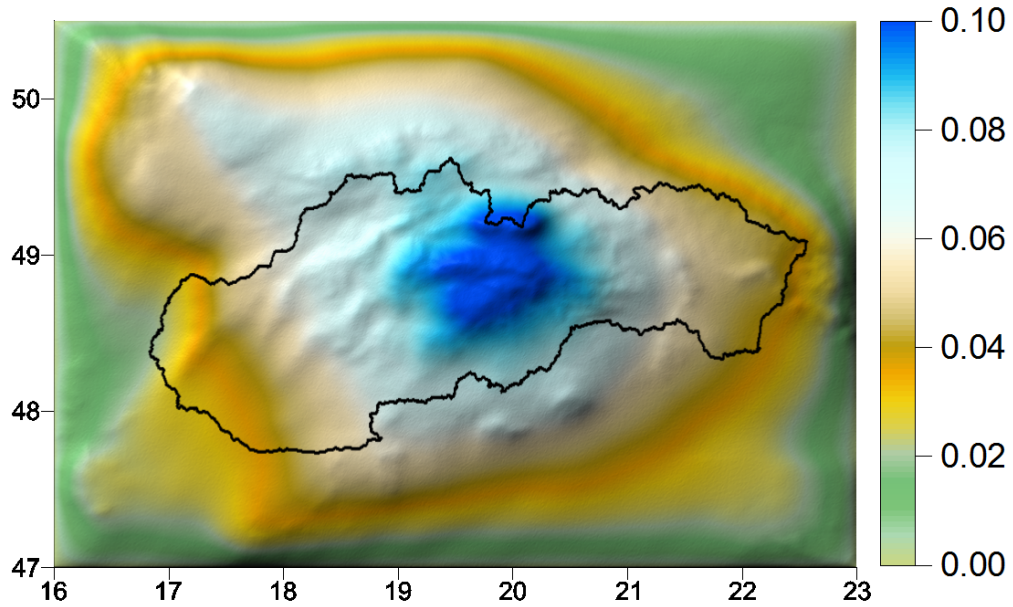


Figure 4.1.3: SR: Differences in  $\zeta[m]$  between the 10<sup>th</sup> and 1<sup>st</sup> iteration obtained by solving the NSFGBVP.

was  $30'' \times 20''$ . Again we started our computations by solving the linearized FGBVP where the surface gravity disturbances were applied on the bottom boundary  $\Gamma$ . They were generated from an available dataset of terrestrial gravity data in Slovakia while ellipsoidal heights of gravimetric measurements were computed from levelling heights using EGM2008. The total gravity  $g$  has been calculated as a sum of the surface gravity disturbance and the normal gravity. On the upper and side boundaries, the disturbing potential generated from the GOCO03s was prescribed. Results obtain by up-wind scheme are presented in Table 4.4 and Fig. 4.1.3. One can observe an improvement in the standard deviation for subsequent iterations in solving the NFGBVP (Tab. 4.4) as well as the convergence to EGM2008. The differences between the 10<sup>th</sup> and 1<sup>st</sup> iteration, which represent the numerically obtained linearization error, reach up to  $10\text{ cm}$ .

	1 <sup>st</sup> iter.	5 <sup>th</sup> iter.	8 <sup>th</sup> iter.	10 <sup>th</sup> iter.	EGM2008
Min. value	0.151	0.209	0.229	0.248	0.301
Mean value	0.284	0.325	0.348	0.352	0.437
Max. value	0.422	0.459	0.476	0.493	0.584
St. deviation	0.055	0.049	0.047	0.046	0.043

Table 4.4: SR: The GPS/levelling test [ $m$ ] for different NFGBVP iterations at 61 points in the area of Slovakia.

	FVM				EGM2008
	Neumann BC	oblique derivative BC		Iterative approach	
		central scheme	up-wind scheme		
Min value	0.045	0.123	0.131	0.248	0.301
Mean value	0.232	0.274	0.279	0.352	0.437
Max value	0.393	0.419	0.421	0.493	0.584
St. deviation	0.076	0.059	0.059	0.046	0.043

Table 4.5: SR: The GPS/leveling test [ $m$ ] at 61 points in area of Slovakia.

# Conclusions

In this dissertation thesis we have presented several approaches for solving geodetic boundary value problems.

In Chapter 1 we have given a brief description of historical background of this problem and we have presented a mathematical formulation of the problems which have been numerically solved, namely

- (i) the non-linear geodetic boundary value problem (GBVP) for the disturbing potential,
- (ii) the GBVP for the disturbing potential with the oblique derivative BC,
- (iii) the GBVP for the disturbing potential with the Neumann BC.

In first part of Chapter 2 we have solved the FGBVP for disturbing potential with the Neumann BC. We have described the finite volume method (FVM) approximation of the Laplace equation together with transmissivity coefficients for spherical domains, proposed in [14]. In comparison to the previous approaches, a new FVM has been developed for solving the problem in ellipsoidal domains. Parallel implementation of the Bi-CGSTAB solver enabled us to solve huge experiments in "*real*" time. Chapter 2 ends with numerical experiments where we have tested experimental order of convergence (EOC) of proposed scheme. We have compared numerical solutions on the spherical and ellipsoidal domain above Himalaya region and obtained all statistical characteristics lower for ellipsoidal domains. Then we have used ellipsoidal computational domain to compute Earth global gravity field and we have showed that standard deviation of

our result and EGM2008 model is in the range of  $2\text{ cm}$ . It indicates high accuracy of our method. We have also performed local experiment in Slovakia and compared our solution with the GPS/levelling test. Such comparison has showed very good accuracy of our results in comparison with other known methods.

In Chapter 3 we have introduced two methods for solving (ii). First method, called the central scheme, is based on splitting of the gradient in normal and tangential directions and the second method, called the up-wind scheme, introduces the oblique derivative BC as an advection equation and uses up-wind principle. By testing numerically central scheme we showed its second order accuracy in several 2D and 3D experiments in contrast with up-wind scheme which is first order accurate. In comparison with previous approach, presented in the Chapter 2, we have achieved better accuracy of both methods in local as well in global gravity field modelling. The standard deviation of residuals at these GPS/levelling points in the case of the FGBVP with the Neumann BC is  $7.6\text{ cm}$ , while in the case of the FGBVP with the oblique derivative BC is only  $5.9\text{ cm}$ .

In last chapter we have proposed an iterative approach for solving (i). In the first iteration, the linearized FGBVP is solved together with the oblique derivative BC. Next iterations treat its numerically obtained linearization error. The obtained numerical results show that the error of the linearization can exceed several centimeters, mainly in high mountainous areas and along ocean trenches. This indicates that for precise gravity field modeling it is necessary to deal with the nonlinear geodetic BVPs avoiding the linearization error. Presented numerical experiments show that the proposed iterative approach converges and that the up-wind method is suitable for an iterative solution. The standard deviation of residuals at these GPS/levelling points in case of the solution to the non-linear FGBVP is only  $4.6\text{ cm}$ .

# Resumé

Jedným z hlavných cieľov fyzikálnej geodézie je učenie ťiažového poľa Zeme. Z matematického pohľadu ide o riešenie Laplaceovej rovnice pre poruchový potenciál mimo Zeme. Ako okrajové podmienky na povrchu Zeme sa najčastejšie uvažujú Newtonove podmienky, reprezentované anomáliami ťiažového zrýchlenia, alebo Neumannove podmienky reprezentované poruchami ťiažového zrýchlenia. V predkladanej práci sme nadviazali na výsledky publikované v [10, 14, 13] a zamerali sme sa na vývoj nových konečno-objemových schém a prístupov k riešeniu problémov fyzikálnej geodézie. Táto práca je rozdelená do štyroch kapitol.

**Prvá kapitola.** V prvej podkapitole uvádzame krátky historický prehľad týkajúci sa geodetickej okrajovej úlohy (GOU). Druhá podkapitola zahŕňa základné matematické vzťahy pre skutočné, normálne a poruchové ťiažové pole. Hlavnou časťou tretej podkapitoly je formulácia GOU pre poruchový potenciál

$$\begin{aligned}\Delta T &= 0 \text{ in } \tilde{\Omega}, \\ |\nabla(T + U)| &= g \text{ na } \Gamma.\end{aligned}$$

Tiež uvažujeme, že poruchový potenciál  $T$  je regulárny v nekonečne

$$T \rightarrow 0 \text{ pre } \mathbf{x} \rightarrow \infty.$$

Po rozpísaní absolútnej hodnoty gradientu vo všeobecnom tvare prepíšeme okrajovú podmienku tak, aby nám umožnila iteračné riešenie úlohy, ktorému sa venujeme detailnejšie v štvrtej kapitole. Prvou iteráciou iteračného predpisu je tzv. linearizovaná fixovaná gravimetrická okrajová úloha [30, 22, 23, 10, 13] so šikmou deriváciou. Pretože je rovnica pre poruchový potenciál definovaná na nekonečnej oblasti, v krátkych úvahách podávame možnosti konštrukcie ohraničenej oblasti  $\Omega$  s odhadom chýb ktorých sa dopúšťame touto modifikáciou pôvodnej úlohy. Následne uvádzame formuláciu modifikovanej GOU (tiež označovanej ako GOU so šikmou deriváciou) v ohraničenej oblasti

$$\begin{aligned}\Delta T &= 0 \text{ in } \Omega, \\ \langle \nabla T, \vec{s} \rangle &= \delta g \text{ na } \Gamma, \\ T &= T_{SAT} \text{ na } \partial\Omega - \Gamma,\end{aligned}$$

a jej riešeniu sa venujeme v tretej kapitole. Poslednou modifikáciou geodetickej okrajovej úlohy, ktorú uvádzame, je prepis okrajovej podmienky cez projekciu šikmého smeru na normálu k hranici

$$\begin{aligned}\Delta T &= 0 \text{ in } \Omega, \\ \frac{\partial T}{\partial n_\Gamma} &= \delta g^* \text{ on } \Gamma, \\ T &= T_{SAT} \text{ on } \partial\Omega - \Gamma.\end{aligned}$$

Riešeniu tejto úlohy je venovaná druhá kapitola. V závere prvej kapitoly sú spomenuté matematické metódy, ktoré sa používajú na riešenie GOU.

**Druhá kapitola.** Ako numerickú metódu na riešenie Laplaceovej rovnice sme si vybrali metódu konečných objemov, ktorej diskretnému prepisu na sférickej a následne i eliptickej oblasti sme venovali začiatok prvej časti druhej kapitoly. Ako sme neskôr

ukázali na numerických experimentoch, eliptická aproximácia je na aproximáciu Zeme vhodnejšia pretože nám umožňuje nám dosiahnuť presnejšie riešenie pre poruchový potenciál. Pretože riešenie poruchového potenciálu je výpočtovo náročná úloha, v ďalšej časti sa venujeme optimalizácii výpočtového procesu. Ako prvé zavádzame nový paralelný riešič Bi-CGSTAB, ktorý v porovnaní s najčastejšie používaným riešičom SOR, konverguje pre dané úlohy rádovo rýchlejšie. Spolu s optimalizáciou spôsobu paralelizácie s využitím NUMA funkcií, sme schopní riešiť väčšie úlohy za kratší výpočtový čas.

Poslednou časťou druhej kapitoly sú numerické experimenty rozdelené na teoretickú a praktickú časť. Teoretické experimenty začíname testovaním chyby ohraničenia výpočtovej oblasti, ktorej veľkosť postupne meníme. Môžeme vidieť, že chyba, ktorá vzniká ohraničením nekonečnej oblasti, klesá so zväčšujúcim sa polomerom hornej hranice oblasti. Zakončením teoretických experimentov sú testy experimentálneho radu konvergenzie, kde ukazujeme, že navrhnutá metóda je druhého rádu. Pre lokálne experimenty sme zvolili oblasť Himalájí a Slovenska. Na oblasti Himalájí ukazujeme vhodnosť voľby eliptickej aproximácie a na globálnom a potom i lokálnom experimente na Slovensku demonštrujeme presnosť výpočtovej metódy v porovnaní s modelom EGM2008.

**Tretia kapitola.** Je venovaná návrhu vhodných algoritmov na riešenie GOU so šikmou deriváciou. Prvá navrhovaná numerická schéma je založená na rozklade gradientu do normálového a tangenciálneho smeru a jej prepisu do 2D

$$\nabla T = \langle \nabla T, \vec{n} \rangle \vec{n} + \langle \nabla T, \vec{t} \rangle \vec{t} = \frac{\partial T}{\partial n} \vec{n} + \frac{\partial T}{\partial t} \vec{t},$$

a 3D

$$\nabla T = \langle \nabla T, \vec{n} \rangle \vec{n} + \langle \nabla T, \vec{t}_1 \rangle \vec{t}_1 + \langle \nabla T, \vec{t}_2 \rangle \vec{t}_2 = \frac{\partial T}{\partial n} \vec{n} + \frac{\partial T}{\partial t_1} \vec{t}_1 + \frac{\partial T}{\partial t_2} \vec{t}_2$$

sa venujeme na začiatku kapitoly. Následné teoretické numerické experimenty ukazujú, že rád konverencie metódy je rovný dvom. Pri experimentoch s reálnymi dátami ukazujeme lepšiu presnosť v porovnaní s riešením úlohy v prvej kapitole. V závere časti o centrálnej schéme poukazujeme na možné problémy pri riešení úloh pomocou tejto aproximácie.

V druhej navrhovanej numerickej schéme predstavujeme okrajovú podmienku ako advektívnu rovnicu riešenú pomocou up-wind schémy, čo nám umožňuje jej prepísanie do tvaru

$$\langle \nabla T, \vec{s} \rangle - \langle T \nabla, \vec{s} \rangle = \delta g.$$

Následným použitím postupov zaužívaných v konečných objemoch dostávame diskrétnu podobu okrajovej podmienky, ktorá má rovnaké vlastnosti ako diskretizácia oblasti. Pri numerických experimentoch ukazujeme, že síce metóda je iba prvého rádu no v porovnaní s centrálnou schémou dosahuje porovnateľné výsledky. V závere kapitoly ukazujeme porovnanie i na reálnych experimentoch.

**Štvrtá kapitola.** V poslednej kapitole sa venujeme iteračnému riešeniu nelineárnej úlohy, kde v každej iterácii riešime šikmú GOU. Ako zastavovaciu podmienku iteračného procesu sme zvolili rezíduum dvoch po sebe idúcich iterácií. Pretože v každej iterácii riešime šikmú GOU, na teoretických experimentoch ukazujeme porovnanie dvoch schém navrhnutých v predchádzajúcej kapitole. Nakoľko v predchádzajúcej kapitole sme ukázali, že obe navrhované metódy na riešenie šikmej GOU dosahujú porovnateľné výsledky a v iteračnom predpise sa up-wind metóda správa stabilnejšie pri experimentoch s reálnymi dátami, ďalej používame iba túto metódu. Ako sme ukázali v reálnych experimentoch iteráciami vieme vylepšiť presnosť riešenia.

**Záver.** V závere uvádzame zhrnutie dosiahnutých výsledkov a záverečné porovnania navrhnutých postupov.

# Bibliography

- [1] Andersen, O.B.: *The DTU10 Gravity field and Mean sea surface*. 2010, Second international symposium of the gravity field of the Earth (IGFS2), Fairbanks, Alaska
- [2] Aoyama, Y. - Nakano, J.: *Practical MPI Programming*. 1999, IBM, [www.redbooks.ibm.com](http://www.redbooks.ibm.com).
- [3] Backus, G.: *Application of a non-linear boundary value problem for Laplace equation to gravity and geomagnetic intensity survey*. 1968, Quarterly Journal of Mechanics and Applied Mathematics, 21, 195-221.
- [4] Barrett, R. - Berry, M.: *Templates of the Solution of Linear System: Building Blocks for Iterative Methods*. 1994, Philadelphia, SIAM.
- [5] Becker, J.J. et al.: *Global Bathymetry and Elevation Data at 30 Arc Seconds Resolution: SRTM30PLUS*. 2009, Marine Geodesy, 32:4, 355-371.
- [6] Bradji, A. - Gallouët, T.: *Error estimate for Finite volume approximate solutions of some oblique derivative boundary value problems*. 2006, International Journal On Finite Volumes, vol. 3, no 2.
- [7] Bradji, A. - Gallouët, T.: *Finite volume approximation for an oblique derivative boundary problem*. 2005, Proceedings of Finite Volume for Complex Applications IV, Hermes. Editors: F. Benkhelhdoun, D. Ouazar and S. Raghay, 143-152.

- [8] Brovar, V.V.: *On the solutions of Molodensky's boundary value problem*. 1964, In Bulletin Géodésique, 72, 167-173.
- [9] Čunderlík, R. - Mikula, K. - Mojzeš, M.: *The boundary element method applied to the determination of the global quasigeoid*. 2000, Proceedings of ALGORITMY 2000, 301 - 308.
- [10] Čunderlík, R. - Mikula, K. - Mojzeš, M.: *Numerical solution of the linearized fixed gravimetric boundary-value problem*. 2008, Journal of Geodesy, Vol. 82, No. 1, 2008, 15 - 29.
- [11] Čunderlík, R. - Mikula, K.: *Direct BEM for high-resolution gravity field modelling*. 2010, Studia Geophysica et Geodetica, Vol. 54, No. 2 , 219-238.
- [12] Eymard, R. - Gallouët, T. - Herbin, R.: *Finite Volume Methods*. 2000, ISBN: 0-444-50350-1, Handbook of Numerical Analysis.
- [13] Fašková, Z. - Čunderlík, R. - Mikula, K.: *Finite element method for solving geodetic boundary value problems*. 2010, Journal of Geodesy, Vol. 84, No. 2, 2010, 135 - 144.
- [14] Fašková, Z.: *Numerical methods for solving geodetic boundary value problem*. 2008, PhD Thesis, SvF STU Bratislava, Slovakia.
- [15] Grafarend, E.W. - Niemeier, W.: *The free nonlinear boundary value problem*. 1971, Bulletin Géodésique, 45, 243-262, 1971.
- [16] Grafarend, E.W.: *The geoid and the gravimetric boundary-value problem*. 1989, Rep. 18 Dept. Geod, The Royal Institute of Technology, Stockholm.
- [17] Grand, T. - Šefara, J. - Pašteka, R. - Bielik, M. - Daniel, S.: *Atlas of geophysical maps and profiles. State geological institute*. 2001, Bratislava, MS Geofond. (in Slovak)

- [18] Han, H. - Wu, X.: *Artificial Boundary Method*. 2013, ISBN-13:978-3-642-35463-2, Springer-Verlag.
- [19] Heck, B.: *On the non-linear geodetic boundary value problem for a fixed boundary surface*. 1989, Bulletin Géodésique, Vol. 63, 57-67.
- [20] Hörmander, L.: *The boundary problems of physical geodesy*. 1976, Archive for Rational Mechanics and Analysis, Vol. 62, 1-52.
- [21] Holota, P.: *Mixed boundary value problems in physical geodesy*. 1982, Proceedings of the symposium 'Figure and dynamics of the earth, moon and planets', Prague 1982.
- [22] Holota, P.: *Coerciveness of the linear gravimetric boundary-value problem and a geometrical interpretation*. 1997, Journal of Geodesy, Vol. 71, No. 10, 640 - 651.
- [23] Holota, P.: *Neumann's boundary-value problem in studies on Earth gravity field: weak solution*. 2005, 50 years of Research Institute of Geodesy, Topography and Cartography, Prague, Vol. 50, No. 36, 49 - 69.
- [24] Holota, P. - Nesvadba, O.: *Model Refinements and Numerical Solutions of Weakly Formulated Boundary-Value Problems in Physical Geodesy*. 2008, Proceedings of VI Hotine-Marussi Symposium on Theoretical and Computational Geodesy, Springer Berlin Heidelberg, 2008.
- [25] Keller, W.: *Finite differences schemes for elliptic boundary value problems*. 1995, Section IV Bulletin IAG, No. 1.
- [26] Klees, R.: *Loesung des fixen geodaetischen Randwertprolems mit Hilfe der Randelementmethode*. 1992, DGK. Reihe C., Nr. 382, Muenchen.
- [27] Klees, R.: *Boundary value problems and approximation of integral equations by finite elements*. 1995, Manuscripta geodaetica, Vol. 20, 345 - 361.

- [28] Klees, R.: *Topics on boundary element methods. Geodetic boundary value problems in view of the one centimeter geoid.* 1998, Lecture Notes in Earth Sciences Vol. 65, Springer, Heidelberg, 482 - 531.
- [29] Klees, R. - Van Gelderen, M. - Lage, C. - Schwab, C.: *Fast numerical solution of the linearized Molodensky problem.* 2001, Journal of Geodesy, Vol. 75, 349 - 362.
- [30] Koch, K.R. - Pope, A.J.: *Uniqueness and existence for the geodetic boundary value problem using the known surface of the earth.* 1972, Bulletin Géodésique, Vol. 46, 467 - 476.
- [31] Lehmann, R.: *Fast space-domain evaluation of geodetic surface integrals.* 1977, Journal of Geodesy, Vol. 71, 533 - 540.
- [32] Lehmann, R. - Klees, R.: *Parallel setup of Galerkin equation system for a geodetic boundary value problem.* 1996, Boundary elements: implementation and analysis of advanced algorithms, Notes on Numerical Fluid Mechanics 54, Vieweg Verlag, Braunschweig.
- [33] Lehmann, R.: *Solving geodetic boundary value problems with parallel computers.* 1997, Geodetic boundary value problems in view of the one centimeter Geoid. Lecture Notes in Earth Sciences vol 65, Springer, Berlin.
- [34] Macák, M. - Mikula, K. - Minarechová, Z. - Čunderlík, R.: *On an iterative approach to solving the nonlinear satellite-fixed geodetic boundary-value problem,* (IAG Symposia Series, in press).
- [35] Macák, M. - Minarechová, Z. - Mikula, K.: *A novel scheme for solving the oblique derivative boundary-value problem* 2014, Studia Geophysica et Geodetica, (published online first).
- [36] Macák, M. - Mikula, K. - Minarechová, Z.: *Solving the oblique derivative boundary-value problem by the finite volume method.* 2012, ALGORITMY 2012, 19th Con-

- ference on Scientific Computing, Podbanske, Slovakia, September 9-14, 2012, Proceedings of contributed papers and posters, Publishing House of STU, 75-84.
- [37] Mayer-Gürr, T.: *The new combined satellite only model GOCO03s*. 2012, Presented at the GGHS-2012 in Venice, Italy.
- [38] Meissl, P.: *The Use of Finite Elements in Physical Geodesy*. 1981, Report 313, Geodetic Science and Surveying, The Ohio State University.
- [39] Mojzeš, M. - Janák, J. - Papčo, J.: *Gravimetric model of Quasigeoid in the area of Slovakia*. 2005, Acta Montanistica Slovaca 10(2), 161-165.
- [40] Molodenskij, M.S. - Jeremejev, B.F. - Jurkina, M.I.: *Methods for study of the external gravitational field and figure of the Earth*. 1962, Israel program for scientific translations, Jerusalem (translated from Russian original, Moscow 1960).
- [41] Moritz, H.: *Nonlinear solutions of the geodetic boundary-value problem*. 1969, Ohio State University, Department of Geodetic Science, report 126.
- [42] Nesvadba, O. - Holota, P. - Klees, R.: *A direct method and its numerical interpretation in the determination of the gravity field of the Earth from terrestrial data*. 2007, Proceedings Dynamic Planet 2005, Monitoring and Understanding a Dynamic Planet with Geodetic and Oceanographic Tools, IAG Symposia Vol. 130, 370-376.
- [43] Pavlis, N.K. - Holmes, S.A. - Kenyon, S.C. - Factor, J.K.: *An Earth Gravitational Model to Degree 2160: EGM2008*. 2008, presented at the 2008 General Assembly of EGU, Vienna, Austria, April 13-18.
- [44] Saad, Y.: *Iterative Methods for Sparse Linear Systems*. 2003, 2nd edition. SIAM, Philadelphia.
- [45] Sacerdote, F. - Sansó, F.: *Overdetermined boundary value problems in physical geodesy*. 1985, Man. Geod., Vol. 10, 195 - 207.

- [46] Sansó, F.: *The geodetic boundary value problem in gravity space*. 1977, Atti della Accademia Nazionale dei Lincei, serie VIII, volume XIV.
- [47] Sleijpen, G.L.G. - Fokkema, D.R.: *Bicgstab(l) for linear equations involving unsymmetric matrices with complex spectrum*. 1993, Electronic Transactions on Numerical Analysis, Vol. 1, pp. 11 - 32.
- [48] Tscherning, C.C. - Knudsen, P. - Forsberg, R.: *Description of the GRAVSOFT package*. 1994, Geophysical Institute, University of Copenhagen, Technical Report, 4th edn.
- [49] Torge, W.: *Geodesy*. 2001, ISBN-13: 978-3110170726, Walter de Gruyter.
- [50] Van der Vorst, H.A.: *Bi-CGSTAB: A Fast and Smoothly Converging Variant of Bi-CG for the Solution of Nonsymmetric Linear Systems*. 1992, SIAM Journal on Scientific Computing, pp.631-644.
- [51] Sideris, M. G. - Schwarz, K. P.: *Solving Molodensky's series by fast Fourier transform techniques*. 1986, Bulletin Geodesique Vol. 60, 51-63.
- [52] Shaofeng, B. - Dingbo, B.: *The finite element method for the geodetic boundary value problem*. 1991, Manuscripta Geodetica Vol.16, 353-359.
- [53] Stokes, G.G.: *On the variation of gravity at the surface of the earth*. 1849, Transactions of the Cambridge Philosophical Society, Section 8, 672-695.
- [54] Wellenhof, B. - Moritz, H.: *Physical Geodesy*. 2006, ISBN: 978-3-211-33545-1, Springer-Verlag.
- [55] Wilford, J.N.: *The mappmakers*. 1981, ISBN: 0375708502, Knopf, New York.

## The author's publications

- Macák, M. - Mikula, K. - Minarechová, Z. - Čunderlík, R.: *On an iterative approach to solving the nonlinear satellite-fixed geodetic boundary-value problem*, (IAG Symposia Series, in press).
- Macák, M. - Minarechová, Z. - Mikula, K.: *A novel scheme for solving the oblique derivative boundary-value problem*. 2014, *Studia Geophysica et Geodetica*, (published online first).
- Macák, M. - Mikula, K.: *Comparison between solutions of the geodetic boundary-value problem with the Neumann and the oblique boundary condition in the area of Himalaya region*. 2013, In: *Advances in Architectural, Civil and Environmental Engineering : 23rd Annual PhD student conference*. Bratislava, SR, 30.10.2013. - Bratislava : Nakladateľstvo STU, 2013. - ISBN 978-80-227-4102-6. - S. 45-50.
- Macák, M. - Mikula, K. - Minarechová, Z.: *Solving the oblique derivative boundary-value problem by the finite volume method*. 2012, In: *ALGORITMY 2012 : 19th Conference on scientific computing. Proceedings*. Podbanské, SR, 9.-14.9.2012. - Bratislava : Nakladateľstvo STU, 2012. - ISBN 978-80-227-3742-5. - S. 75-84.
- Macák, M. - Fašková, Z. - Čunderlík, R. - Mikula, K.: *Solution of the geodetic boundary value problem by the finite volume method over an ellipsoid*. 2012, In: *Juniorstav 2012 [elektronický zdroj] : 14. odborná konferencia doktorského štúdia s mezinárodnou účasťou*. Brno, 26.1.2012. - Brno : Vysoké učení technické v Brně, 2012. - ISBN 978-80-214-4393-8.
- Macák, M. - Fašková, Z. - Čunderlík, R. - Mikula, K.: *Latest improvements in solution of the geodetic boundary value problem by the finite volume method*. 2011, In: *MAGIA 2011 : Mathematics, geometry and their applications. Proceedings*,

Kočovce, SR, 28.-30.10.2011. - Bratislava : Nakladateľstvo STU, 2012. - ISBN  
978-80-227-3780-7. - S. 14-21.